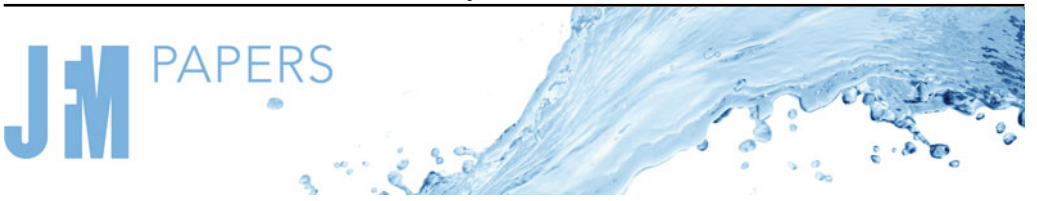
J. Fluid Mech. (2025), *vol.* 1022, A38, doi:10.1017/jfm.2025.10771



Oscillatory flows in three-dimensional deformable microchannels

Anxu Huang[1,†], **Shrihari D. Pande**[2,†], **Jie Feng**[1] and **Ivan C. Christov**[2]

[1]Department of Mechanical Science and Engineering, University of Illinois Urbana–Champaign, Urbana, IL 61801, USA

[2]School of Mechanical Engineering, Purdue University, West Lafayette, IN 47907, USA

Corresponding authors: Ivan C. Christov, christov@purdue.edu; Jie Feng, jiefeng@illinois.edu

(Received 8 April 2025; revised 5 August 2025; accepted 28 September 2025)

Deformable microchannels emulate a key characteristic of soft biological systems and flexible engineering devices: the flow-induced deformation of the conduit due to slow viscous flow within. Elucidating the two-way coupling between oscillatory flow and deformation of a three-dimensional (3-D) rectangular channel is crucial for designing lab-on-a-chip and organ-on-a-chip microsystems and eventually understanding flow–structure instabilities that can enhance mixing and transport. To this end, we determine the axial variations of the primary flow, pressure and deformation for Newtonian fluids in the canonical geometry of a slender (long) and shallow (wide) 3-D rectangular channel with a deformable top wall under the assumption of weak compliance and without restriction on the oscillation frequency (i.e. on the Womersley number). Unlike rigid conduits, the pressure distribution is not linear with the axial coordinate. To validate this prediction, we design a polydimethylsiloxane-based experimental platform with a speaker-based flow-generation apparatus and a pressure acquisition system with multiple ports along the axial length of the channel. The experimental measurements show good agreement with the predicted pressure profiles across a wide range of the key dimensionless quantities: the Womersley number, the compliance number and the elastoviscous number. Finally, we explore how the nonlinear flow–deformation coupling leads to self-induced streaming (rectification of the oscillatory flow). Following Zhang and Rallabandi (*J. Fluid Mech.*, vol. 996, 2024, p. A16), we develop a theory for the cycle-averaged pressure based on the primary problem's solution, and we validate the predictions for the axial distribution of the streaming pressure against the experimental measurements.

[†] These authors contributed equally.

© The Author(s), 2025. Published by Cambridge University Press. This is an Open Access article, distributed under the terms of the Creative Commons Attribution-NonCommercial-ShareAlike licence (https://creativecommons.org/licenses/by-nc-sa/4.0/), which permits non-commercial re-use, distribution, and reproduction in any medium, provided the same Creative Commons licence is used to distribute the re-used or adapted article and the original article is properly cited. The written permission of Cambridge University Press must be obtained prior to any commercial use.

https://doi.org/10.1017/jfm.2025.10771 Published online by Cambridge University Press

Key words: microfluidics, lubrication theory, flow-vessel interactions

1. Introduction

Fluid–structure interactions (FSIs) between oscillatory internal viscous fluid flows and their deformable confining boundaries are ubiquitous across natural and engineered systems and across scientific disciplines. For example, such FSIs arise in biomedical problems involving blood circulation (Pedley 1980; Fung 1997) in the cardiovascular system (van de Vosse & Stergiopulos 2011; Menon, Hu & Marsden 2024), specifically the large arteries (Ku 1997; Grotberg & Jensen 2004; Čanić *et al.* 2005), as well as flows in the vocal cords (Heil & Hazel 2011), lungs (Grotberg 1994; Grotberg & Jensen 2004; Heil & Hazel 2011), brain (Bork *et al.* 2023; Gan *et al.* 2023), retina (Stewart & Foss 2019) and synovial joints (Dowson & Jin 1986; Parthasarathy, Bhosale & Gazzola 2022). Harnessing these FSIs has proven critical for the design and construction of microfluidic devices (Leslie *et al.* 2009; Mosadegh *et al.* 2010; Xia *et al.* 2021; Battat, Weitz & Whitesides 2022; Biviano *et al.* 2022; Mudugamuwa *et al.* 2024), which has enabled emerging technologies such as organs-on-chips (Bhatia & Ingber 2014; Lind *et al.* 2017; Dalsbecker, Beck Adiels & Goksör 2022; Leung *et al.* 2022), flexible and wearable electronics (Jeong, Bychkov & Searson 2018; Kwon *et al.* 2023) and soft robotics (Elbaz & Gat 2014; Matia, Elimelech & Gat 2017; Gamus *et al.* 2018; Matia *et al.* 2023; Xu *et al.* 2023). The deformation of compliant conduits by oscillatory flows also arises in elastohydrodynamic lubrication (Karan, Chakraborty & Chakraborty 2021; Rallabandi 2024) and at scales relevant to geophysical problems (Kurzeja *et al.* 2016; Rodríguez de Castro *et al.* 2023). While oscillatory (and/or pulsatile) viscous flows (Zamir 2000) in elastic tubes is a time-honoured subject, dating back to Womersley's work in the 1950s (Womersley 1955*a*,*b*), the two-way-coupled interplay between the pressure gradient driving the flow and the deformation of the compliant wall has, surprisingly, not been fully explored, as a series of recent works highlighted (Pande, Wang & Christov 2023; Zhang & Rallabandi 2024; Krul & Bagchi 2025).

The initial impetus for understanding the fluid mechanics of oscillatory flow was that 'the central problem in haemodynamics flow ... [was not] satisfactorily resolved for arterial flow' (McDonald 1955). This 'central problem', initially defined by Burton (1952) as 'the relation of pressure to flow', has been a cornerstone in studies focusing on the flow rate–pressure drop ($q-\Delta p$) relationship of oscillatory internal flows, starting with the fundamental study by Womersley (1955*b*). However, despite significant progress, much of the literature has focused on the case of one-way coupling between flow and deformation, namely how the flow and structure behave if the pressure gradient is considered known *a priori*, as assumed by Womersley (1955*a*,1957). Furthermore, prior experimental investigations of such internal periodic flows in compliant conduits generally focused on biomedical applications. For example, Pielhop *et al.* (2012, 2015) and Dörner *et al.* (2021) used 'time-resolved particle-image velocimetry combined with a wall detection algorithm and non-invasive pressure measurements' to study the biofluid mechanics of large elastic polydimethylsiloxane (PDMS) vessels under moderate- to high-Reynolds-number conditions, including for a non-Newtonian blood-analogue fluid. However, these studies lacked theoretical support to rationalise their observations. Most recently, Krul & Bagchi (2025) performed detailed simulations of the two-way-coupled FSI between an oscillatory flow and a thin viscoelastic shell, with the analysis and interpretation guided by Womersley's classical theory.

https://doi.org/10.1017/jfm.2025.10771 Published online by Cambridge University Press

Returning to the microfluidic context, the resistance of channels of various cross-sectional shapes is well understood (Bruus 2008). Recently, significant progress has been made in developing the $q-\Delta p$ relationship for two-way-coupled steady flows through deformable conduits at low Reynolds number (Christov 2022), while the same is not true for similar oscillatory flows. As Dincau, Dressaire & Sauret (2020) note, 'pulsatile microfluidics is still in its infancy', especially when it comes to wall compliance. In the context of low-Reynolds-number flows, Anand & Christov (2020) and Pande *et al.* (2023) revisited the problem of two-way-coupled FSI between oscillatory flows and elastic channels and tubes, showing (through asymptotic analysis, modelling and direct numerical simulations) the existence of a secondary (streaming) flow resulting from the nonlinear coupling between pressure and deformation at low Reynolds number. This streaming effect represents a type of self-induced peristaltic pumping mechanism, which is a topic extensively studied in biomechanics (see e.g. Takagi & Balmforth 2011; Amselem, Clanet & Benzaquen 2023, and references therein). The opposite problem of an external flow driven by oscillations of an elastic body, termed soft streaming, was considered by Bhosale, Parthasarathy & Gazzola (2022) and Cui, Bhosale & Gazzola (2024). Lambert (1958) and Ling & Atabek (1972) argued that, for flows in arteries, both the advective nonlinearity of the Navier–Stokes equations and the geometric and material nonlinearity of the elastic wall should be taken into account. Ling & Atabek (1972) provided limited comparisons between experimental measurements of velocity, flow rate and shear stress and simulations via a reduced-order model as support. Indeed, the complete theory by Zhang & Rallabandi (2024) of the elastoinertial rectification mechanism, underlying the streaming flow observed by Pande *et al.* (2023), shows that advective inertia is inextricably coupled to pressure and deformation in these flows, but using linear elastic theories (e.g. thin-shell theory in Zhang & Rallabandi (2024)) suffices in the context of microfluidic flows. However, the non-zero cycle-averaged pressure (due to the nonlinear coupling between flow inertia and wall deformation) has not been systematically measured in an experiment.

The desire to fill this knowledge gap in the field of nonlinear microfluidics (Xia *et al.* 2021; Battat *et al.* 2022) motivates the present combined theoretical–experimental study. Specifically, we develop a microfluidic experimental platform consisting of a test section with a compliant wall and multiple pressure ports. To drive the flow, we develop a custom pressure-generation system capable of delivering a wide range of frequencies and amplitudes with precise control. This experimental platform enables us to characterise the spatiotemporal pressure distribution due to the oscillatory flow of Newtonian fluids in three-dimensional (3-D) deformable microchannels, including measuring the weak cycle-averaged (streaming) pressure. To guide and rationalise the experiments, we extend the axisymmetric theory of Zhang & Rallabandi (2024) to 3-D slender and shallow deformable channels, which are commonly encountered in experimental microfluidic systems (Gervais *et al.* 2006; Cheung, Toda-Peters & Shen 2012; Ozsun, Yakhot & Ekinci 2013; Mehboudi & Yeom 2019; Paludan *et al.* 2024).

The rest of this paper is organised as follows. In § 2, we introduce the problem, governing equations, scales and dimensionless numbers and apply the lubrication approximation. In § 3, we describe the experimental set-up for the oscillatory flow generation and methodology for pressure measurement. In § 4, we perform a perturbation expansion for weak compliance to obtain the primary flow, pressure and wall displacement profiles for a Newtonian fluid in such a slender and shallow deformable 3-D channel, as well as the streaming pressure distribution along the channel. We cross-validate our results through quantitative comparisons between experimental pressure measurements and theoretical predictions in § 5. Conclusions and perspectives for future work are summarised in § 6.

https://doi.org/10.1017/jfm.2025.10771 Published online by Cambridge University Press

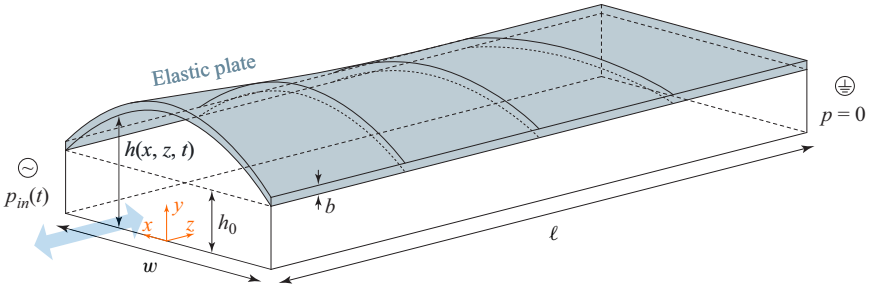


Figure 1. Schematic of the 3-D deformable shallow and slender rectangular microchannel geometry of initial (undeformed) height h_0, axial length ℓ and transverse width w, such that $\ell \gg w \gg h_0$. The top wall (darker colour) is an elastic plate structure of thickness b that can deform from $y = h_0$ to $y = h(x, z, t)$, where $h(x, z, t) - h_0 = u_y(x, z, t)$ is the vertical displacement of the fluid–solid interface. The top wall is clamped (no displacement) along the planes $x = \pm w/2$ (and $0 \leqslant z \leqslant \ell$), while taking the outlet pressure as gauge, $p|_{z=\ell} = 0$, ensures no deformation along the plane $z = \ell$ (and $-w/2 \leqslant x \leqslant +w/2$). An oscillatory inlet pressure, $p|_{z=0} = p_{in}(t)$ of amplitude p_0 and angular frequency ω, drives the flow.

2. Oscillatory flow in a slender and shallow 3-D deformable channel

Consider the oscillatory flow of a Newtonian fluid with constant density ρ_f and constant dynamic viscosity μ_f through a 3-D rectangular channel of initial height h_0, transverse width w and axial length ℓ, shown schematically in figure 1, as commonly encountered in experimental microfluidic systems. The flow is driven by inlet pressure oscillations of magnitude p_0 and angular frequency ω. The velocity field is $\boldsymbol{v} = (v_x, v_y, v_z)$ and the pressure field is p. The bottom ($y = 0$) and side ($x = \pm w/2$) walls are rigid, but the top wall can deform. The deformable top wall is made from a linearly elastic material with Young's modulus E and Poisson's ratio ν_s. The displacement field of the top wall is given by $\boldsymbol{u} = (u_x, u_y, u_z)$.

2.1. *Governing equations of the oscillatory flow*

In this context, Martínez-Calvo *et al.* (2020) analysed the inertialess startup flow, following on from the steady problem solved by Christov *et al.* (2018), introducing scalings that balance all velocity components in the conservation of mass equation. Ramos-Arzola & Bautista (2021) also used these scalings for a non-Newtonian version of the problem. Here, unlike these prior works, we adopt the scaling of the 3-D problem introduced by Boyko & Christov (2023), which leads to a leading-order problem that can be spanwise-averaged. Although both approaches are valid within the assumed order of approximation for a shallow and wide channel, only the latter approach allows us to make analytical progress in the oscillatory flow problem. Specifically, we scale both cross-sectional velocities, v_x and v_y, so that they are smaller than the axial one, v_z, by a factor of $\epsilon \overset{\text{def}}{=} h_0/\ell$, where $\epsilon \ll 1$ for a slender channel.

With all this in mind, we introduce the dimensionless variables for the problem:

$$X = \frac{x}{w}, \quad Y = \frac{y}{h_0}, \quad Z = \frac{z}{\ell}, \quad T = \frac{t}{\omega^{-1}}, \quad V_X = \frac{v_x}{\epsilon v_c}, \quad V_Y = \frac{v_y}{\epsilon v_c},$$
$$V_Z = \frac{v_z}{v_c}, \quad P = \frac{p}{p_0}, \quad U_X = \frac{u_x}{u_c}, \quad U_Y = \frac{u_y}{u_c}, \quad U_Z = \frac{u_z}{u_c}, \quad H = \frac{h}{h_0}. \tag{2.1}$$

Here, p_0 and ω are the amplitude and angular frequency, respectively, of the inlet pressure oscillations driving the flow. The scales v_c and u_c for the axial velocity and wall displacement, respectively, are determined below. In terms of the dimensionless

https://doi.org/10.1017/jfm.2025.10771 Published online by Cambridge University Press

variables from (2.1), the governing partial differential equations (PDEs) of leading-order-in-ϵ unsteady flow in a 3-D channel (i.e. a slender channel under the lubrication approximation for which $\epsilon \ll 1$ (Leal 2007)) are

$$\delta\frac{\partial V_X}{\partial X}+\frac{\partial V_Y}{\partial Y}+\frac{\partial V_Z}{\partial Z}=0, \tag{2.2a}$$

$$0=-\frac{\partial P}{\partial X}, \tag{2.2b}$$

$$0=-\frac{\partial P}{\partial Y}, \tag{2.2c}$$

$$Wo^2\left[\frac{\partial V_Z}{\partial T}+\frac{\beta}{\gamma}\left(\delta V_X\frac{\partial V_Z}{\partial X}+V_Y\frac{\partial V_Z}{\partial Y}+V_Z\frac{\partial V_Z}{\partial Z}\right)\right]=-\frac{\partial P}{\partial Z}+\delta^2\frac{\partial^2 V_Z}{\partial X^2}+\frac{\partial^2 V_Z}{\partial Y^2}, \tag{2.2d}$$

where we have chosen the axial velocity scale as $v_c = h_0^2 p_0/(\ell\mu_f)$ to balance viscous and pressure forces in (2.2*d*). In scaling the problem this way, several key dimensionless numbers emerge:

$$\delta \overset{\text{def}}{=} \frac{h_0}{w}, \tag{2.3a}$$

$$Wo^2 \overset{\text{def}}{=} \frac{h_0^2/(\mu_f/\rho_f)}{\omega^{-1}} = \frac{\text{transverse momentum diffusion time scale}}{\text{oscillation time scale}}, \tag{2.3b}$$

$$\beta \overset{\text{def}}{=} \frac{u_c}{h_0} = \frac{\text{top wall displacement scale}}{\text{initial channel height}}, \tag{2.3c}$$

$$\gamma \overset{\text{def}}{=} \frac{u_c/(\epsilon v_c)}{\omega^{-1}} = \frac{\text{elastoviscous time scale}}{\text{oscillation time scale}}. \tag{2.3d}$$

Here, δ is the channel's cross-sectional (inverse) aspect ratio ($\delta \ll 1$ for wide channels); β is the compliance number (Christov *et al.* 2018), where wall displacement scale u_c is introduced below upon specifying the elasticity model; Wo is the Womersley number (Womersley 1955*a*); and γ is the elastoviscous number (Elbaz & Gat 2014; Zhang & Rallabandi 2024), where the elastoviscous time scale emerges from comparing the vertical displacement scale u_c (set by elasticity) with the vertical velocity scale ϵv_c (set by the balance of viscous and pressure forces). For a stiff top channel wall (weakly compliant channel), we would expect $\beta \ll 1$. On the other hand, we do not impose any restrictions on γ or *Wo a priori*. Although it may be tempting to rewrite β/γ in (2.2*d*) as a Reynolds number (Pande *et al.* 2023), it will become clear below why that is not a good idea (Zhang & Rallabandi 2024).

Now, assuming a wide (shallow) channel, $\delta \ll 1$, so that we can neglect all terms at $O(\delta)$ and higher in (2.2), we have

$$\frac{\partial V_Y}{\partial Y}+\frac{\partial V_Z}{\partial Z}=0, \tag{2.4a}$$

$$0=-\frac{\partial P}{\partial X}, \tag{2.4b}$$

$$0=-\frac{\partial P}{\partial Y}, \tag{2.4c}$$

$$Wo^2\left[\frac{\partial V_Z}{\partial T}+\frac{\beta}{\gamma}\left(V_Y\frac{\partial V_Z}{\partial Y}+V_Z\frac{\partial V_Z}{\partial Z}\right)\right]=-\frac{\partial P}{\partial Z}+\frac{\partial^2 V_Z}{\partial Y^2}. \tag{2.4d}$$

As usual, from (2.4*b*,*c*), we immediately conclude that $P = P(Z, T)$ only.

https://doi.org/10.1017/jfm.2025.10771 Published online by Cambridge University Press

The flow obeys no-slip and no-penetration conditions along the bottom wall of the channel:

$$V_Z|_{Y=0} = 0, \quad V_Y|_{Y=0} = 0. \tag{2.5a,b}$$

Along the deformable (thus, moving) top wall, $y = h(x, z, t)$, a kinematic condition, $\boldsymbol{v} = D\boldsymbol{u}/Dt$, applies. In dimensionless component form, the kinematic condition is

$$V_X|_{Y=H} = \left(\gamma \frac{\partial U_X}{\partial T} + \frac{u_c}{w} V_X \frac{\partial U_X}{\partial X} + \frac{u_c}{h_0} V_Y \frac{\partial U_X}{\partial Y} + 0\right)\Bigg|_{Y=H}, \tag{2.6a}$$

$$V_Y|_{Y=H} = \left(\gamma \frac{\partial U_Y}{\partial T} + \frac{u_c}{w} V_X \frac{\partial U_Y}{\partial X} + \frac{u_c}{h_0} V_Y \frac{\partial U_Y}{\partial Y} + 0\right)\Bigg|_{Y=H}, \tag{2.6b}$$

$$V_Z|_{Y=H} = O(\epsilon), \tag{2.6c}$$

having used the third condition to simplify the first two. Further simplification can only be obtained upon specifying the governing equations of the wall deformation (in § 2.2). Since we restrict ourselves to pressure-driven flows (as described in more detail in § 3), the inlet and outlet pressures are known:

$$P|_{Z=0} = P_{in}(T), \quad P|_{Z=1} = 0. \tag{2.7a,b}$$

2.2. *Governing equations of the top wall deformation*

Assuming a thin structure, we employ plate theory. The central tenet of plate theory is that the structure is thin and thus the vertical displacement u_y (in the thin direction) does not vary with y (Reddy 2007). Thus, the bottom surface of the top wall (i.e. the fluid–solid interface) is located at $h_0 + u_y$ upon deformation of the wall (see figure 1).

Anand, Muchandimath & Christov (2020) provide a full derivation and discussion of the equations of motion of slender and shallow thick plates obeying the theory due to Reissner (1945) and Mindlin (1951), which governs the flexural deformation of isotropic, elastic plates deduced from the 3-D equations of elasticity when the plate's thickness is non-trivial – a so-called first-order shear deformation theory (Reddy 2007; Challamel & Elishakoff 2019). Here, we summarise the key details. The in-plane plane displacements are given by $u_x = u_x^0(x, z) + \bar{y}\phi_x(x, z)$ and $u_z = u_z^0(x, z) + \bar{y}\phi_z(x, z)$, where ϕ_x and ϕ_z are rotations of the normal vector to the plate's midsurface about the x and z axes, respectively, and $\bar{y}$ is measured from the midsurface, i.e. $\bar{y} = y - h_0 - b/2$. The PDEs for $u_x^0(x, z)$ and $u_z^0(x, z)$ decouple from those for $\phi_y(x, z)$, $\phi_z(x, z)$ and $u_y(x, z)$. In the absence of external in-plane loads, these PDEs are homogeneous. Thus, from the clamped boundary conditions (BCs) (as in figure 1), it follows that $u_x^0 = u_z^0 \equiv 0$. Consequently, the plate problem reduces to determining the vertical displacement, u_y, and the rotations of the normal, ϕ_x and ϕ_z. A balancing argument shows that the appropriate scales for ϕ_x and ϕ_z are u_c/w and u_c/ℓ, respectively.

For a slender and shallow plate, neglecting terms of $O(\delta)$ and $O(\epsilon)$, Φ_Z drops out of the governing plate equations, which now feature only U_Y and Φ_X (Anand *et al.* 2020). Our starting point is these equations, at the leading order in δ and ϵ, namely

$$St_s \frac{\partial^2 U_Y}{\partial T^2} = \frac{1}{720} \frac{\partial^3 \Phi_X}{\partial X^3} + P(Z, T), \tag{2.8a}$$

$$0 = \Phi_X + \frac{\partial U_Y}{\partial X} - \frac{\mathscr{T}}{60} \frac{\partial^2 \Phi_X}{\partial X^2}, \tag{2.8b}$$

https://doi.org/10.1017/jfm.2025.10771 Published online by Cambridge University Press

where $\mathscr{T} \overset{\text{def}}{=} 10(b/w)^2/(1-\nu_s)$ is a dimensionless parameter quantifying the shallowness of the plate. Having balanced transverse bending with the pressure load from the flow in (2.8*a*), $u_c = w^4 p_0/(720 D_b)$, where $D_b = Eb^3/[12(1-\nu_s^2)]$ is the flexural rigidity of a plate in pure bending (Reddy 2007), E is Young's modulus and ν_s is Poisson's ratio. The factor of $1/720$ included in u_c might not be obvious now; it is included to eliminate all numerical prefactors in (4.6) below.

Similar to Martínez-Calvo *et al.* (2020), we have retained the displacement's inertia in (2.8*a*), but neglected rotary inertia in (2.8*b*) as is standard in the literature (see e.g. Zienkiewicz, Taylor & Zhu (2013), Chap. 13). The inertia of the plate is thus quantified by the solid's Strouhal number:

$$St_s \overset{\text{def}}{=} \frac{\rho_s b u_c/p_0}{\omega^{-2}} = \frac{(\text{solid's time scale for response to loading})^2}{(\text{oscillation time scale})^2}, \tag{2.9}$$

where ρ_s is the density of the elastic wall material.

Generalising the steady results of Shidhore & Christov (2018), (2.8) describe transverse bending of the wall, i.e. the deformation in any (X, Y) plane for fixed Z, subject to the normal load imposed by the hydrodynamic pressure $P(Z, T)$. The axial tension and bending are neglected as they scale with $\epsilon \ll 1$ (Anand *et al.* 2020). The corresponding clamped BCs supplementing (2.8) are

$$U_Y|_{X=\pm 1/2} = 0, \quad \Phi_X|_{X=\pm 1/2} = 0. \tag{2.10a,b}$$

Observe that if we let $\mathscr{T} \to 0$ (i.e. $b/w \to 0$), then $\Phi_X = -\partial U_Y/\partial X$ from (2.8*b*), and substituting this relation into (2.8*a*) and (2.10*b*) reduces these to the corresponding equation of Kirchhoff–Love (thin-plate) theory (see e.g. Howell, Kozyreff & Ockendon 2009).

Finally, based on this discussion, we have deduced that $U_X = O(\delta)$ and $U_Z = O(\epsilon)$. Thus, the in-plane displacements are negligible compared with the vertical (out-of-plane) displacement U_Y at leading order, which significantly simplifies the kinematic condition (2.6).

2.3. *Coupling flow to deformation*

Since the in-plane displacements U_X and U_Z are negligible, the dimensionless kinematic condition (2.6) reduces to three independent BCs. The X and Z components, (2.6*a*) and (2.6*c*), are essentially no-slip BCs: $V_X|_{Y=H} = V_Z|_{Y=H} = 0$. While the Y component (2.6*b*) dictates that the fluid's vertical velocity matches that of the wall:

$$V_Y|_{Y=H} = \frac{\gamma}{\beta}\frac{\partial H}{\partial T}, \tag{2.11}$$

where $H(X, Z) = 1 + \beta U_Y(X, Z)$ is the dimensionless height of the fluid channel. We recognise that γ/β can also be interpreted as a fluidic Strouhal number (Ramachandra Rao 1983; Ward & Whittaker 2019; Inamdar, Wang & Christov 2020; Pande *et al.* 2023). Equation (2.11) is key to the two-way coupling of the flow and deformation.

Next, we seek to manipulate the kinematic condition (2.11) into one involving the flow rate. To this end, we define the flow rate Q by integrating over the cross-sectional area in an (X, Y) plane:

$$Q = \int_{-1/2}^{+1/2} \int_0^H V_Z \, \mathrm{d}Y \mathrm{d}X. \tag{2.12}$$

https://doi.org/10.1017/jfm.2025.10771 Published online by Cambridge University Press

Dimensionless number	Notation/expression	Assumption	Typical value/range
Channel's slenderness	$\epsilon = h_0/\ell$	Negligible	0.008
Channel's shallowness	$\delta = h_0/w$	Negligible	0.08
Womersley	$Wo = h_0\sqrt{\rho_f \omega/\mu_f}$	None	0.5−3.2
Elastoviscous	$\gamma = w^4\ell^2\mu_f\omega/(720 D_b h_0^3)$	None	0.15−15
Compliance	$\beta = w^4 p_0/(720 D_b h_0)$	Small	0.01−0.2
Solid's inertial Strouhal	$St_s = \rho_s b w^4\omega^2/(720 D_b)$	Negligible	1.7×10^{-6}−1.4×10^{-3}
Plate's shallowness	$\mathscr{T} = 10(b/w)^2/(1-\nu_s)$	Small	0.03−0.138

Table 1. Key dimensionless numbers of the 3-D elastoinertial rectification problem, based on the characteristic displacement scale u_c for a plate and a characteristic axial velocity scale v_c under lubrication theory. Typical values/ranges are based on the experimental set-up (§ 3). Negligible numbers are taken as zero in the analysis (i.e. the theory is 'at leading order' in these parameters), while small quantities are taken into account; perturbatively in the case of β.

Then, a lengthy but straightforward calculation using the Leibniz rule to swap the order of Y integration and Z differentiation shows that the kinematic BC (2.11) can be combined with (2.12) to re-express the conservation of mass (2.4*a*) as the continuity equation:

$$\frac{\partial Q}{\partial Z} + \frac{\gamma}{\beta}\frac{\partial}{\partial T}\int_{-1/2}^{+1/2}\left[1+\beta U_Y(X,Z,T)\right]\mathrm{d}X = 0. \tag{2.13}$$

2.4. *Summary of the governing equations and dimensionless numbers*

In summary, (2.4*d*), (2.8) and (2.13) are the governing equations of the oscillatory flow in a 3-D shallow and slender channel with a plate-like deformable top wall in pure bending.

The key dimensionless groups of the problem are summarised in table 1. The experimental system, discussed next in § 3, was designed to achieve an oscillatory flow with $Wo, \gamma = O(1)$ in the weakly compliant regime β small (but not negligible) in a slender $\epsilon \ll 1$ and shallow $\delta \ll 1$ channel, which are the key approximations made in the theoretical analysis. These considerations lead to the parameter values/ranges given in table 1. Additionally, we learn from table 1 that the channels constructed have negligible wall inertia, $St_s \ll 1$, allowing us to consider the plate deformation as quasi-static.

3. Experimental set-up

3.1. *Oscillatory flow generation and shaping*

Our experimental set-up is shown in figure 2. Previous experimental investigations of oscillatory flow generation in microchannels (Pielhop, Klaas & Schröder 2015; Raj *et al.* 2019; Vishwanathan & Juarez 2020; Dörner *et al.* 2021; Levenstein *et al.* 2022; Vishwanathan & Juarez 2022, 2023) involved synchronising mechanical vibrations directly to the fluid itself in a microfluidic channel. Notably, the way that Vishwanathan & Juarez (2020, 2022, 2023) achieved this is by attaching an inlet tube to the diaphragm of a speaker, such that the fluid within the channel was driven by the oscillations initiated from the inlet tube, ultimately creating an oscillatory flow. Inspired by this approach, we customised our oscillatory flow generation module as follows. We utilised a function generator (GH-CJDS66, Koolertron) connected with a speaker (DR-US200275, Drok) to ensure a robust signal input. We further introduced a PDMS (Sylgard 184, Dow Corning) liquid chamber positioned towards the speaker, with its membrane linked to the speaker

https://doi.org/10.1017/jfm.2025.10771 Published online by Cambridge University Press

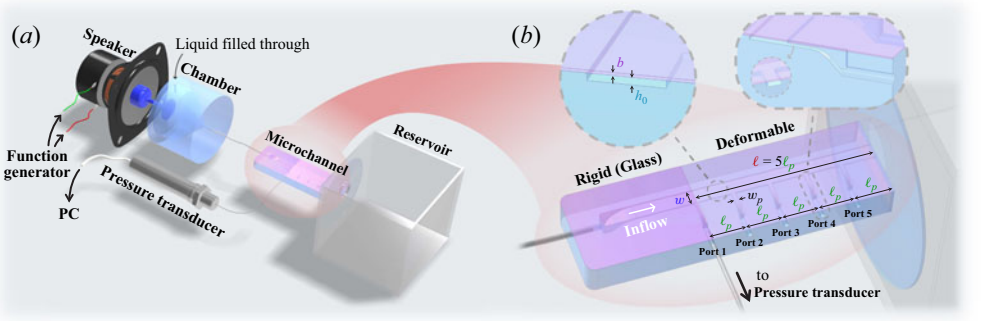


Figure 2. Experimental system with oscillatory flow in a 3-D deformable rectangular microchannel. (*a*) Set-up schematic. The entire interior space of the system is completely filled with the fluid prior to the experiments. To initiate the flow, an analogue sinusoidal signal generated by the function generator is transmitted into the speaker, enabling its diaphragm to vibrate. The deformable membrane of the liquid chamber (linked to the speaker diaphragm via a rigid, 3-D-printed connector shown in dark blue) transmits these vibrations, causing the oscillation of the fluid within both the chamber and the following channel. (*b*) Microchannel configuration. The channel features five pressure ports connecting to the data acquisition system (pressure transducer and PC). The five ports (each of width w_p) are evenly spaced with an axis-to-axis interval ℓ_p in the flow direction. The microchannel section between the first port and the outlet is covered with a deformable PDMS film of length ℓ at the top, and the section of the channel ahead of the first port is covered by a rigid glass slide, with its front edge precisely aligned to the centre of the first port.

diaphragm via a rigid, 3-D-printed connector to facilitate efficient mechanical vibration transmission. The chamber was first fabricated using 3-D-printed moulding techniques, and the membrane (with thickness of the order of 0.5 mm) sealing the liquid chamber was then bonded by inverting the chamber onto a liquid layer of PDMS mixture, which was subsequently cured at 90 °C for one hour to ensure solidification and secure adhesion. All PDMS components were fabricated with a 10:1 (w/w) ratio of silicone elastomer base to curing agent.

In each experiment, this chamber was filled with the working fluid to generate sufficient pressure amplitude. Once the analogue sinusoidal signal from the function generator was transmitted into the speaker, which enabled its diaphragm to vibrate, the connected deformable membrane of the chamber thereby vibrated, causing the fluid oscillations inside the chamber and transmitting them to the microchannel. Before each experiment, we carefully eliminated any entrapment of air within the entire interior space, such as air pockets in all pressure ports and tubing, which is found to be important for obtaining reliable pressure amplitudes by the pressure transducer. In addition, the microchannel outlet was submerged in a liquid reservoir filled with the working fluid slightly above the level of the microchannel to maintain a constant hydrostatic pressure at the outlet, which is approximately atmospheric pressure given the small height.

3.2. *Fabrication of the microchannels with deformable top walls*

To fabricate the rectangular microchannel with deformable top walls, we follow the same procedure as Chun *et al.* (2024), where a 3-D-printing technique (Mars Resin 3D Printer, ELEGOO, USA) was employed to manufacture the reverse mould with the designated channel dimensions as listed in table 2. A mixing ratio of 10:1 (w/w) between the silicone elastomer base and the curing agent was used to prepare the PDMS elastomer. The PDMS mixture was subsequently poured into the 3-D-printed mould and degassed under vacuum for 1 h to fully remove entrapped air bubbles. The mixture was then cured in

https://doi.org/10.1017/jfm.2025.10771 Published online by Cambridge University Press

Microchannel				
h_0 (mm)	w (mm)	ℓ (mm)	ℓ_p (mm)	w_p (mm)
0.50 ± 0.005	5.0 ± 0.05	60.0 ± 0.25	12.0 ± 0.05	1.4 ± 0.05
Deformable top walls				
b (mm)	E (MPa)	ν_s	ρ_s (kg m^{-3})	
0.43 ± 0.01	1.02 ± 0.05	0.47 ± 0.1	1070 ± 10	
0.20 ± 0.005	1.21 ± 0.02			

Table 2. Dimensions of the microchannel and elastic properties of the deformable walls.

an oven at 90 °C for 24 h. Upon curing, the PDMS block as the channel substrate was carefully detached from the mould, followed by the fluid inlet and pressure measurement ports being precisely punctured by a 2 mm disposable biopsy punch. To probe the time-varying pressure distribution along the flow direction, the five ports (spaced ℓ_p apart; see figure 2*b*) were designed to connect to a pressure transducer for pressure measurements along the channel. All ports (with width w_p at the branching point where they intersect with the main channel) were located to the side of the channel (figure 2*b*) for convenient experimental operation. The lateral cross-sectional view of the entire port is shown in the inset of figure 2(*b*). Additionally, a smooth geometric transition following an elliptic arc was employed at the microchannel inlet to minimise any secondary flows created at sharp corners.

Two thin PDMS films were used as the deformable top walls. One PDMS film with a thickness of 0.43 ± 0.01 mm was fabricated in the laboratory following the procedure of Chun *et al.* (2024). The other PDMS film (GASKET-UT-200PK) with a thickness of 0.2 ± 0.005 mm was purchased from SIMPore Inc., USA. The films and microchannel substrate were treated with a 4.5 MHz hand-held corona treater (BD-20AC, Electro-Technic Products, USA) for 30 s, and then we brought the film and the channel substrate together into conformal contact for bonding. We note that this bonding approach for oscillatory flows was proven to be robust, as confirmed by the reproducibility of our experiments. We further attached a rigid glass slide on top of the thin PDMS film, other than the section between the first port and the outlet, to confine the deformability solely to this section. We confirmed all dimensions of the channel and the thin PDMS film by microscope visualisation (table 2). We also measured the Young's modulus E and Poisson's ratio ν_s of the thin PDMS film using dynamic mechanical analysis (Q800 DMA, TA instruments, USA) at a room temperature of 20 °C. For the PDMS films that we fabricated in the laboratory, the measurements of the Young's moduli were performed after 24 h to ensure the material properties of the PDMS films were fully stabilised. The density ρ_s from the datasheet is reported.

To validate our experimental system for oscillatory flows, we also fabricated a rigid microchannel, which is the counterpart of the deformable microchannels with the same dimensions and configuration, except that the top wall was replaced by a large PDMS block. Using the same fabrication procedures as for the channel substrate, the PDMS block was fabricated to be as thick as the channel substrate (thickness ≈ 1 cm), ensuring that its rigidity prevents any deformation under the typical imposed hydrodynamic pressure (amplitude ≈ 0.1 kPa) used for the experiments with the thin-film top walls. Subsequently, the large PDMS block was attached to its dedicated channel substrate by undergoing the same surface treatment as for the thin-film top walls described above.

https://doi.org/10.1017/jfm.2025.10771 Published online by Cambridge University Press

Fluid	ρ_f (kg m^{-3})	μ_f (mPa s)
Deionised water	1000 ± 1	1 ± 0.05
50 wt% glycerine solution	1115 ± 1.1	6 ± 0.3

Table 3. Physical properties of the working fluids.

3.3. *Working fluids and pressure measurements*

Two different viscous Newtonian fluids, deionised water and an aqueous solution of 50 wt% glycerine, were used to tune the Womersley number Wo and the elastoviscous number γ. The working fluids' densities and viscosities are reported in table 3, which were measured right before each experiment. The viscosity of the working fluids was quantified by flow sweep tests performed using a stress-controlled rheometer (DHR-3, TA Instruments, USA).

For the pressure measurement, the gauge pressure at each pressure port was recorded by a pressure transducer (PX409-10WGUSBH, OMEGA, USA) wired to the PC with control software (Digital Transducer Application, OMEGA, USA), using a sampling rate of 1000 Hz for all cases, which is much larger than the frequency of the pressure signal in our experiments (typically set between 1 and 16 Hz). Prior to each experiment, the pressure transducer was calibrated using a column of water. Then, the entire interior space of the system, including the tubing connected to the pressure transducer, was completely filled with the working fluid. Thereafter, the top opening of the PDMS chamber (used to fill it with fluid) was kept closed, and the channel outlet was completely submerged under the free surface of the fluid in the reservoir. The five pressure ports were also blocked by the tubing connected to the pressure transducer and four plugs to maintain a hermetically sealed liquid environment.

We measured the pressure distribution of both the primary flow (derived in § 4.1) and the secondary streaming flow (derived in § 4.2). For the primary flow, we synchronised the pressure's time variation in each port with one pressure transducer as follows. At the onset of each experiment, the function generator was configured to produce a sinusoidal waveform with a predetermined frequency and voltage. As the speaker diaphragm continuously oscillated under the excitation of the function generator, pressure variations over time were recorded. For a given pressure input, characterised by an amplitude and frequency, we first recorded data at the first port, $p_1(t) = p(z_1, t)$, as shown in figure 2(*b*) (hereafter referred to as 'port 1') for a sufficiently long duration. Next, to synchronise the $p_i(t)$ data of port i (where $i = 2$, 3, 4 or 5) onto the time axis of port 1's data under the same pressure input, we implemented a staged recording method for port i. First, we began the data collection on port 1. Second, we transferred the pressure sampling tube from port 1 to port i. Third, we continued data collection at port i before concluding the session. This entire process was completed within the total duration of port 1's data acquisition in the first session. To align the pressure datasets, we applied a temporal adjustment by shifting the whole $p_i(t)$ curve of the second session along the time axis until its initial time slot measuring port 1 precisely overlapped with port 1's reference data from the first session, eliminating any phase discrepancy. This approach ensured that the data recorded for each port were accurately synchronised with the time axis established by port 1's dataset. The same procedure was systematically repeated for all pressure measurement ports, ultimately yielding a fully synchronised pressure dataset across all five ports for a given pressure input.

https://doi.org/10.1017/jfm.2025.10771 Published online by Cambridge University Press

On the other hand, to measure the weak streaming pressure in the secondary flow for each pressure port, we first obtained a baseline pressure value with no flow (the speaker off), then recorded the pressure signal with the flow (the speaker on). The difference between the cycle-averaged value of the pressure signal with the flow and the baseline pressure reflects the streaming effect therein. We used these pressure differences to further calculate the cycle-averaged streaming pressure, which, in this case, was the sole measurement in which we are ultimately interested, meaning the synchronisation between ports was not critical.

4. Theory of elastoinertial rectification in a 3-D deformable channel

The oscillatory flow has a time-harmonic (zero-mean) component called the primary flow. Nonlinearity, due to two-way coupling between the flow and deformation as well as flow inertia, induces a secondary flow. This secondary flow can have a non-zero mean component, which is often referred to as a streaming flow. Classically, streaming is studied in the context of viscous flows in which weak advective inertia provides the nonlinearity. The latter example is referred to as acoustic streaming (Riley 1998, 2001; Sadhal 2012). Either way, if a zero-mean forcing produces a non-zero net cycle-averaged flow, we say that the oscillatory flow experiences rectification.

For internal flows in conduits, a non-zero mean flow can be produced by a slowly varying conduit cross-section (e.g. the radius in a tube) or by curvature (twists and turns) of the conduit in the flow direction (Pedley 1980). Streaming flows can also be generated by peristalsis (small-amplitude waves propagated along the conduit wall), with applications to microelectromechanical systems (Selverov & Stone 2001) and biofluid mechanics (Romanò *et al.* 2020; Trevino *et al.* 2025). In the present context of an internal flow in a deformable channel, the streaming flow arises from the combination of geometric (flow-induced elastic deformation) and inertial nonlinearities.

To decouple the primary and secondary flows, we follow Zhang & Rallabandi (2024) and expand all variables in a perturbation series in $\beta \ll 1$,

$$\{V_Y,\, V_Z,\, Q,\, P\} = \underbrace{\{V_{Y,0},\, V_{Z,0},\, Q_0,\, P_0\}}_{\text{primary flow}} + \beta\, \underbrace{\{V_{Y,1},\, V_{Z,1},\, Q_1,\, P_1\}}_{\text{secondary flow}} + O(\beta^2), \tag{4.1}$$

without restricting γ or Wo. Below, we construct the primary flow solution explicitly (§ 4.1), while for the secondary flow, we only evaluate the cycle-averaged (i.e. streaming or rectified) component (§ 4.2).

4.1. *Primary flow: $O(1)$ solution*

Substituting the expansion (4.1) into the momentum equations (2.4*b*) and (2.4*c*), we find that the primary pressure P_0 does not vary with X or Y. Then, at $O(1)$, the Z-momentum equation (2.4*d*) and the no-slip BCs from (2.5*a*) and (2.6*c*) become

$$\left.\begin{aligned} Wo^2 \frac{\partial V_{Z,0}}{\partial T} &= -\frac{\mathrm{d}P_0}{\mathrm{d}Z} + \frac{\partial^2 V_{Z,0}}{\partial Y^2}, \\ V_{Z,0}|_{Y=0} &= V_{Z,0}|_{Y=1} = 0. \end{aligned}\right\} \tag{4.2}$$

We expect the primary flow to be harmonic; thus, we introduce phasors: $V_{Z,0}(Y, Z, T) = \mathrm{Re}[V_{Z,0,a}(Y, Z)\mathrm{e}^{\mathrm{i}T}]$ and $P_0(Z, T) = \mathrm{Re}[P_{0,a}(Z)\mathrm{e}^{\mathrm{i}T}]$. Substituting the phasors into (4.2),

https://doi.org/10.1017/jfm.2025.10771 Published online by Cambridge University Press

the solution for the axial velocity phasor's amplitude is easily found (see e.g. Pande *et al.* 2023) to be

$$V_{Z,0,a}(Y,\,Z) = \frac{1}{\mathrm{i}Wo^2}\left[1 - \frac{\cos\left(\mathrm{i}^{3/2}(1-2Y)Wo/2\right)}{\cos\left(\mathrm{i}^{3/2}Wo/2\right)}\right]\left(-\frac{\mathrm{d}P_{0,a}}{\mathrm{d}Z}\right). \tag{4.3}$$

Now, the flow rate phasor's amplitude is evaluated by substituting (4.3) into (2.12) to yield

$$\left.\begin{aligned} Q_{0,a} &= \int_{-1/2}^{+1/2}\int_0^1 V_{Z,0,a}\,\mathrm{d}Y\,\mathrm{d}X = \mathfrak{f}(Wo)\left(-\frac{\mathrm{d}P_{0,a}}{\mathrm{d}Z}\right), \\ \mathfrak{f}(Wo) &\overset{\text{def}}{=} \frac{1}{\mathrm{i}Wo^2}\left[1 - \frac{1}{\mathrm{i}^{3/2}Wo/2}\tan\left(\mathrm{i}^{3/2}Wo/2\right)\right]. \end{aligned}\right\} \tag{4.4}$$

Next, we determine the top wall displacement. Having verified that $St_s \ll 1$, we neglect the wall's inertia. Then, the solution of (2.8) subject to the BCs (2.10) (see e.g. Shidhore & Christov 2018) is

$$U_Y(X,\,Z,\,T) = 30\left(\frac{1}{4} - X^2\right)\left[\left(\frac{1}{4} - X^2\right) + \frac{\mathscr{T}}{5}\right]P(Z,\,T). \tag{4.5}$$

Substituting (4.5) into (2.13), performing the X integration and then substituting the perturbation expansions for Q and P in terms of phasors, the continuity equation becomes

$$\frac{\mathrm{d}Q_{0,a}}{\mathrm{d}Z} + (1+\mathscr{T})\,\gamma\mathrm{i}P_{0,a}(Z) = 0. \tag{4.6}$$

Finally, substituting the flow rate–pressure gradient relation (4.4) into the continuity equation (4.6), and taking into account the pressure BCs (2.7), we arrive at a boundary-value problem (BVP) for the primary pressure amplitude:

$$\left.\begin{aligned} &\mathfrak{f}(Wo)\frac{\mathrm{d}^2P_{0,a}}{\mathrm{d}Z^2} = \mathrm{i}\,(1+\mathscr{T})\,\gamma\,P_{0,a}(Z), \\ &P_{0,a}(0) = 1, \quad P_{0,a}(1) = 0. \end{aligned}\right\} \tag{4.7}$$

Here, according to the experimental system's set-up, we have taken $P_{in}(T) = \mathrm{Re}[\mathrm{e}^{\mathrm{i}T}] + O(\beta)$, having imposed the amplitude of the pressure oscillations as the characteristic pressure scale via (2.1). We have left open the possibility of $O(\beta)$ corrections to the oscillatory pressure BC, which may arise from how the oscillatory flow was generated in the experiments. We return to this issue in § 4.2.

The solution to the BVP (4.7) is easily found to be

$$P_{0,a}(Z) = \frac{\sinh\left(\kappa(1-Z)\right)}{\sinh\kappa}, \quad \kappa = \kappa(Wo,\,\gamma,\,\mathscr{T}) \overset{\text{def}}{=} \sqrt{\frac{\mathrm{i}\,(1+\mathscr{T})\,\gamma}{\mathfrak{f}(Wo)}}, \tag{4.8a,b}$$

which has the same form as the corresponding solution in an axisymmetric deformable tube (Ramachandra Rao 1983; Dragon & Grotberg 1991; Zhang & Rallabandi 2024). This solution is illustrated in figure 3. We observe that $\kappa/\sqrt{(1+\mathscr{T})\gamma}$ is solely a function of Wo with asymptotics of $\sim\sqrt{3\mathrm{i}}(2+\mathrm{i}Wo^2/10)$ as $Wo\to 0$ and $\sim\sqrt{\mathrm{i}}(1+\sqrt{\mathrm{i}Wo})$ as $Wo\to\infty$. The large-Wo asymptotics show a much faster ($\sim Wo$) growth for the 3-D rectangular channel compared with the 3-D axisymmetric tube ($\sim\sqrt{Wo}$) in Zhang & Rallabandi (2024).

https://doi.org/10.1017/jfm.2025.10771 Published online by Cambridge University Press

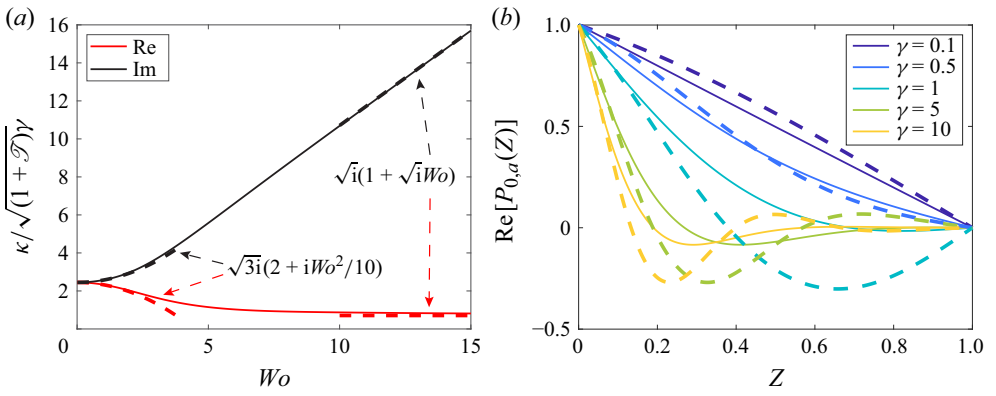


Figure 3. (*a*) Dependence of the reduced complex 'wavenumber' $\kappa/\sqrt{(1+\mathscr{T})\gamma}=\sqrt{\mathrm{i}\mathfrak{f}(Wo)}$ on Wo and its asymptotic behaviours (dashed curves labelled with arrows). (*b*) Shape of the primary pressure amplitude's axial distribution, $\mathrm{Re}[P_{0,a}(Z)]$ from (4.8*a*), for $Wo=1$ (solid) and $Wo=3$ (dashed) and across a range of γ values.

Observe that as the elastoviscous adjustment of the wall becomes instantaneous compared with the oscillation time scale ($\gamma\to 0$), i.e. the channel is effectively rigid, then $\kappa\to 0$ and $P_{0,a}(Z)\to 1-Z$ from (4.8), as expected.

4.2. *Secondary flow: $O(\beta)$ solution*

To define the secondary (streaming) flow problem, we must determine the axial velocity at the deformable wall in terms of known quantities. Following Boyko, Stone & Christov (2022), we proceed by domain perturbation (Lebovitz 1982; Leal 2007). To this end, recall that $H=1+\beta U_Y=1+\beta U_{Y,0}+O(\beta^2)$, and expand the axial velocity at the wall in a Taylor series:

$$V_Z|_{Y=H}=V_{Z,0}|_{Y=1}+\beta U_{Y,0}\left.\frac{\partial V_{Z,0}}{\partial Y}\right|_{Y=1}+\beta V_{Z,1}|_{Y=1}+O(\beta^2). \tag{4.9}$$

Enforcing the no-slip BC $V_Z|_{Y=H}=0$ due to (2.6*c*), (4.9) requires that

$$V_{Z,0}|_{Y=1}=0,\quad V_{Z,1}|_{Y=1}=-\,U_{Y,0}\left.\frac{\partial V_{Z,0}}{\partial Y}\right|_{Y=1}. \tag{4.10a,b}$$

Observe that the flow-induced deformation of the channel leads to an effective slip velocity $V_{Z,1}|_{Y=1}$ in (4.10*b*) along the original location of the wall (Anand & Christov 2020; Zhang & Rallabandi 2024).

Since we are interested only in the streaming (or rectified) flow component, we now apply the cycle-averaging operator $\langle\,\cdot\,\rangle\overset{\text{def}}{=}(1/2\pi)\int_0^{2\pi}(\,\cdot\,)\,\mathrm{d}T$ to (2.4*d*) and (2.13) at $O(\beta)$ to obtain

$$\frac{Wo^2}{\gamma}\left\langle V_{Y,0}\frac{\partial V_{Z,0}}{\partial Y}+V_{Z,0}\frac{\partial V_{Z,0}}{\partial Z}\right\rangle=-\frac{\mathrm{d}\langle P_1\rangle}{\mathrm{d}Z}+\frac{\partial^2\langle V_{Z,1}\rangle}{\partial Y^2}, \tag{4.11a}$$

$$\frac{\partial\langle Q_1\rangle}{\partial Z}=0. \tag{4.11b}$$

Observe that the left-hand side of (4.11*a*) is independent of X, and so is $\langle P_1\rangle$ (due to the cycle-averaged (2.4*b*) at $O(\beta)$). Thus, we can X-average the $O(\beta)$ problem's governing

https://doi.org/10.1017/jfm.2025.10771 Published online by Cambridge University Press

equation (4.11):

$$\frac{Wo^2}{\gamma}\left\langle V_{Y,0}\frac{\partial V_{Z,0}}{\partial Y}+V_{Z,0}\frac{\partial V_{Z,0}}{\partial Z}\right\rangle=-\frac{\mathrm{d}\langle P_1\rangle}{\mathrm{d}Z}+\frac{\partial^2\langle\!\langle V_{Z,1}\rangle\!\rangle}{\partial Y^2}, \tag{4.12a}$$

$$\frac{\partial\langle\!\langle Q_1\rangle\!\rangle}{\partial Z}=0, \tag{4.12b}$$

where $\langle\!\langle\,\cdot\,\rangle\!\rangle\overset{\text{def}}{=}(1/2\pi)\int_{-1/2}^{+1/2}\int_0^{2\pi}(\,\cdot\,)\,\mathrm{d}T\,\mathrm{d}X$ denotes the simultaneous T and X averaging. The T averages involving $O(1)$ phasors $\mathcal{A}=\mathrm{Re}[\mathcal{A}_a\mathrm{e}^{\mathrm{i}T}]$ and $\mathcal{B}=\mathrm{Re}[\mathcal{B}_a\mathrm{e}^{\mathrm{i}T}]$ are calculated by the standard rule $\langle\mathcal{A}\mathcal{B}\rangle=(1/2)\mathrm{Re}[\mathcal{A}_a^*\mathcal{B}_a]=(1/2)\mathrm{Re}[\mathcal{A}_a\mathcal{B}_a^*]$, where a star superscript denotes complex conjugate.

Four conditions are required to simultaneously and uniquely determine $\langle\!\langle V_{Z,1}\rangle\!\rangle$, $\langle\!\langle Q_1\rangle\!\rangle$ and $\langle P_1\rangle$ from (4.12). The suitable BCs now correspond to no slip at $Y=0$ (from averaging (2.5*a*)) and effective slip at $Y=1$ (from averaging (4.10*b*)):

$$\langle\!\langle V_{Z,1}\rangle\!\rangle|_{Y=0}=0,\quad \langle\!\langle V_{Z,1}\rangle\!\rangle|_{Y=1}=-\left\langle\!\left\langle U_{Y,0}\frac{\partial V_{Z,0}}{\partial Y}\right|_{Y=1}\right\rangle\!\right\rangle. \tag{4.13a,b}$$

The conditions in the experiment are such that the membrane in the liquid-filled chamber used for oscillatory flow generation (recall figure 2) does not allow any net flow through the system. Then, according to (4.12*b*), $\langle\!\langle Q_1\rangle\!\rangle=\text{const.}$, and this constant must be zero throughout. The outlet is open to the gauge pressure per (2.7). Thus, the remaining BCs are

$$\langle\!\langle Q_1\rangle\!\rangle|_{Z=0}=0,\quad \langle P_1\rangle|_{Z=1}=0. \tag{4.14a,b}$$

Using (4.5), the slip velocity becomes

$$\left\langle\!\left\langle U_{Y,0}\frac{\partial V_{Z,0}}{\partial Y}\right|_{Y=1}\right\rangle\!\right\rangle=\left\langle\int_{-1/2}^{+1/2}U_{Y,0}\,\mathrm{d}X\;\frac{\partial V_{Z,0}}{\partial Y}\right|_{Y=1}\Bigg\rangle=\left\langle(1+\mathscr{T})P_0\frac{\partial V_{Z,0}}{\partial Y}\right|_{Y=1}\Bigg\rangle. \tag{4.15}$$

It is convenient to now rewrite $\langle\!\langle V_{Z,1}\rangle\!\rangle$ in a way to eliminate the pressure gradient on the right-hand side of (4.12*a*) and simultaneously satisfy the slip BC (4.13*b*). Specifically, let

$$\langle\!\langle V_{Z,1}\rangle\!\rangle(Y,Z)=-\frac{1}{2}\frac{\mathrm{d}\langle P_1\rangle}{\mathrm{d}Z}Y(1-Y)-Y(1+\mathscr{T})\left\langle P_0\frac{\partial V_{Z,0}}{\partial Y}\right|_{Y=1}\Bigg\rangle+\widetilde{\langle\!\langle V_{Z,1}\rangle\!\rangle}(Y,Z). \tag{4.16}$$

Then, substituting (4.16) into (4.12*a*), we obtain a new BVP for $\widetilde{\langle\!\langle V_{Z,1}\rangle\!\rangle}$, subject to homogeneous BCs:

$$\left.\begin{aligned}&\frac{Wo^2}{\gamma}\left\langle V_{Y,0}\frac{\partial V_{Z,0}}{\partial Y}+V_{Z,0}\frac{\partial V_{Z,0}}{\partial Z}\right\rangle=\frac{\partial^2\widetilde{\langle\!\langle V_{Z,1}\rangle\!\rangle}}{\partial Y^2},\\&\widetilde{\langle\!\langle V_{Z,1}\rangle\!\rangle}|_{Y=0}=\widetilde{\langle\!\langle V_{Z,1}\rangle\!\rangle}|_{Y=1}=0.\end{aligned}\right\} \tag{4.17}$$

An analytical solution appears unlikely since the left-hand side of the ordinary differential equation in (4.17) is a complicated, complex-valued function of Y and Z, but some useful approximations are discussed in Appendix A. Instead, we solve the linear two-point BVP (4.17) numerically using Matlab's `bvp4c` subroutine, which implements a finite-difference solver with residual-based error control (Kierzenka & Shampine 2001), with absolute and relative tolerance of 10^{-6}.

https://doi.org/10.1017/jfm.2025.10771 Published online by Cambridge University Press

Finally, from (4.12*b*), (4.14*a*) and (4.16), we conclude that

$$\langle\!\langle Q_1 \rangle\!\rangle = \int_0^1 \langle\!\langle V_{Z,1} \rangle\!\rangle \, \mathrm{d}Y = -\frac{1}{12}\frac{\mathrm{d}\langle P_1 \rangle}{\mathrm{d}Z} + \mathfrak{Q}(Z) = 0, \tag{4.18}$$

where, for convenience, we have let

$$\mathfrak{Q}(Z) \overset{\text{def}}{=} \underbrace{-\frac{1}{2}(1+\mathscr{T})\left\langle P_0 \frac{\partial V_{Z,0}}{\partial Y}\bigg|_{Y=1}\right\rangle}_{\text{from effective slip}} + \underbrace{\int_0^1 \widetilde{\langle\!\langle V_{Z,1} \rangle\!\rangle} \, \mathrm{d}Y}_{\text{from advective inertia}} . \tag{4.19}$$

Equation (4.18) is a first-order differential equation for the streaming pressure $\langle P_1 \rangle$ subject to the outlet BC (4.14*b*), which is easily solved to obtain

$$\langle P_1 \rangle(Z) = -12 \int_Z^1 \mathfrak{Q}(\tilde{Z}) \, \mathrm{d}\tilde{Z}. \tag{4.20}$$

In the experiment, the membrane in the liquid-filled chamber used for oscillatory flow generation imposes a weak, $O(\beta)$, non-zero mean pressure at the inlet, which is consistent with (4.20). To plot $\langle P_1 \rangle(Z)$, we evaluate $\mathfrak{Q}(Z)$ from (4.19) wherein the integral over Y is computed numerically using the trapezoidal rule via Matlab's `trapz` with $\Delta Y = 0.0101$ from the numerical solution for $\widetilde{\langle\!\langle V_{Z,1} \rangle\!\rangle}$ of BVP (4.17). Then, the indefinite integral in (4.20) is evaluated numerically using Matlab's `cumtrapz` using $\Delta Z = 0.0204$.

5. Comparison between experiment and theory

To make the comparison between the experimental measurements (§ 3) and the primary and streaming pressure distributions predicted by the theory (§ 4), we first post-processed the experimental data. To isolate the primary pressure oscillations and set the gauge pressure to zero, the mean of the signal was removed. Then, we fitted the oscillatory pressure experimental data from the inlet pressure sensor 1 to a sinusoidal waveform of the form $p_1(t) = p_0 \cos(2\pi f_{true}(t - t_{tshift}))$, where p_0 is the amplitude of the pressure signal we seek to determine, f_{true} is the 'true' frequency of the signal (slightly shifted from the input waveform frequency f due to imperfections in the system) and t_{shift} is a phase introduced by the fact that the experimental data capture does not have to start right at a peak or trough of the sinusoidal signal. To find p_0, we applied Matlab's `findpeaks` subroutine to the zero-mean signal, and the values it returned were averaged to obtain p_0. Then, f_{true} and t_{shift} were found using `findfit`. After p_0 and f_{true} were successfully identified for a given experiment, the key dimensionless numbers (table 1) were calculated and used to evaluate the theoretical predictions.

5.1. *Validation in a rigid channel*

To validate the experimental system, we first assessed its performance using a rigid channel ($\gamma = 0$) with deionised water as the working fluid. This validation is accomplished by comparing the experimental pressure data for the rigid channel with the $\gamma \to 0$ limit of the theory, which gives $P(Z, T) = \mathrm{Re}[(1 - Z)\mathrm{e}^{\mathrm{i}T}]$ from (4.8). We considered three validation cases with different input frequencies (corresponding to $Wo = 2.5$, 3.32 and 3.96). The case of $Wo = 2.5$ is shown as an example in figure 4. We observe good agreement between the theory and experiments for the axial distribution of P and its variation over time in figure 4(*b*). The same holds for the other two validation experiments (not shown).

Note that the experimental pressure data time series (figure 4*a*) does not show any phase difference between the pressure signals at the different axial positions, which

https://doi.org/10.1017/jfm.2025.10771 Published online by Cambridge University Press

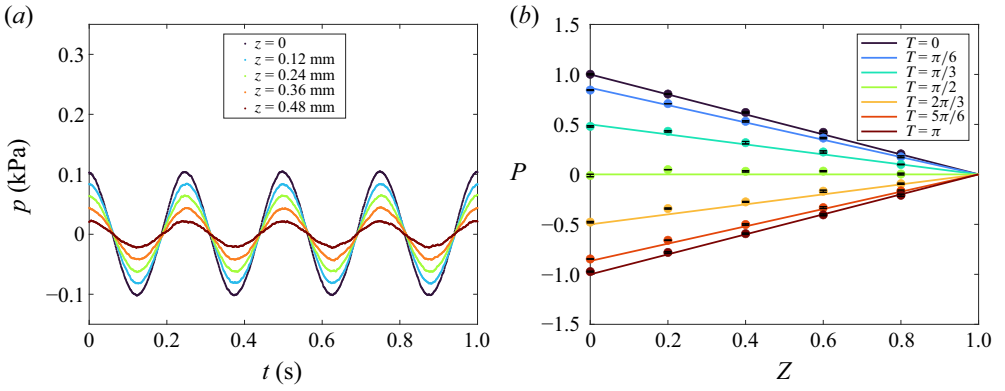


Figure 4. Pressure distribution and evolution in a rigid channel ($\gamma = 0$) with $Wo = 2.5$. (*a*) Experimental time series of the evolution of the pressure over time at the different axial positions of the ports (recall figure 2*b*). (*b*) Comparison between the evolution of the dimensionless axial pressure distribution from the experiments (symbols) and the rigid-channel theory (solid lines) over half a cycle.

is to be contrasted with the results for the deformable channel below (§ 5.2). The signals' amplitudes exhibit a trend of linear attenuation with z, characterised by a constant multiplicative relationship between the values at different z. Correspondingly, in figure 4(*b*), these observations are reflected in the linear variation of P with Z at every T over half an oscillation cycle.

5.2. *Comparison of primary pressure oscillations in deformable channels*

Next, we turn to the experiments in the deformable channels, based on a 50 wt% glycerine solution as the working fluid. In this subsection, we discuss the primary (purely oscillatory) pressure (§ 4.1) in the compliant channel. In figure 5, we show the experimentally measured pressure evolution at each of the different pressure ports for four pairs of values of the Womersley and compliance numbers – a low value $Wo = 0.537$ (slow flow oscillation) and a high value $Wo = 2.15$ (fast flow oscillation), as well as two different orders of magnitude of β, namely $\simeq 10^{-2}$ and $\simeq 10^{-1}$. To change the compliance number β, the thickness of the deformable top wall was varied in the experiments (recall table 2). In figure 5, the mean pressure has been subtracted to set the outlet pressure as the gauge and to make the signal purely oscillatory.

Comparing the pressure time series in figure 5 (e.g. figure 5*b*) with time series in the rigid channel in figure 4(*a*), we observe a distinct phase difference developing between the time series collected at different z (i.e. at different pressure ports). Furthermore, the decrease in the signals' amplitudes is not proportional in the deformable channel, unlike in the rigid channel. These differences are expected to arise from the nonlinear two-way coupling of the flow and deformation (increasing β).

To clearly demonstrate the nonlinear coupling, in figure 6, we compare the dimensionless primary pressure distribution $P_0(Z, T) = \mathrm{Re}[P_{0,a}(Z)\mathrm{e}^{\mathrm{i}T}]$ from (4.8) predicted by the theory with the experimental data. We neither construct $P_1(Z, T)$, which is not straightforward (Zhang & Rallabandi 2024), nor neglect its $O(\beta)$ contribution, as we have ensured a one-to-one comparison of primary theoretical and experimental pressures by removing the mean of the experimental time series. Notably, unlike the steady (Christov *et al.* 2018) and startup (Martínez-Calvo *et al.* 2020) problems, the key dimensionless groups influencing the pressure distribution in the deformable channel are the Womersley number Wo and the elastoviscous number γ, not the compliance number β.

https://doi.org/10.1017/jfm.2025.10771 Published online by Cambridge University Press

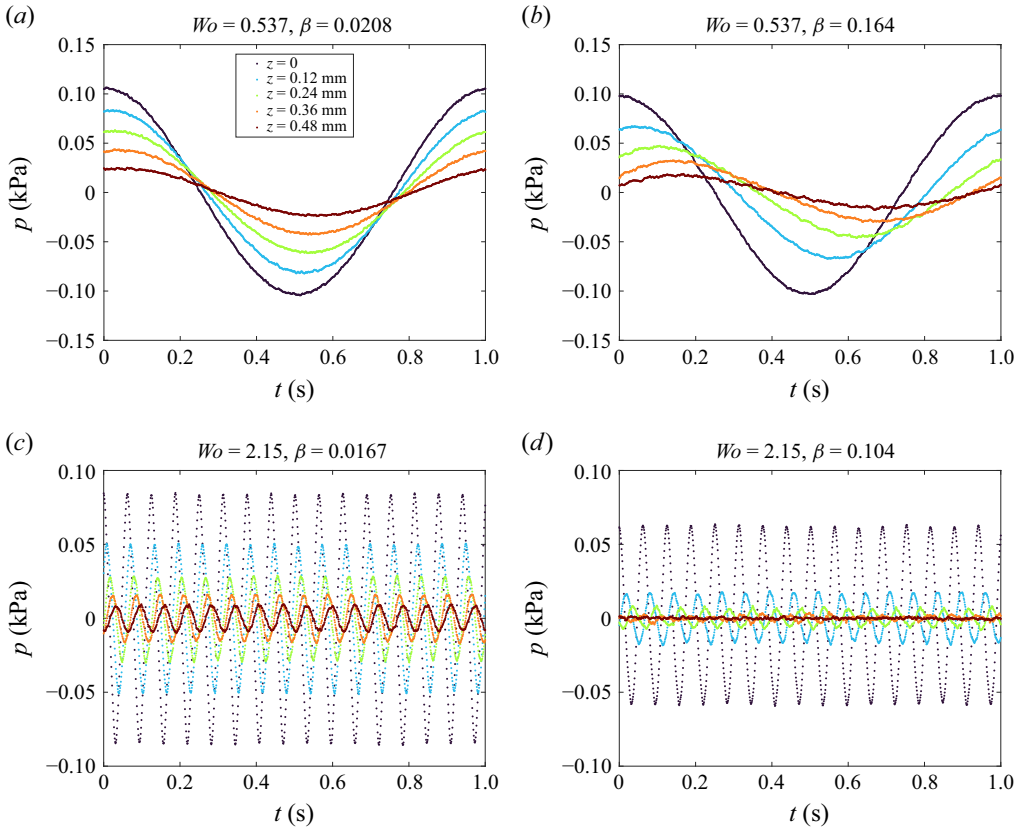


Figure 5. Experimental measurements of the evolution of the pressure over time at different axial positions (pressure port locations) for the deformable channel for smaller and larger compliance numbers (left-hand column versus right-hand column) and smaller and larger Womersley numbers (top row versus bottom row). Specifically, (*a*) $Wo = 0.537$ ($\gamma = 0.109$), (*b*) $Wo = 0.537$ ($\gamma = 0.913$), (*c*) $Wo = 2.15$ ($\gamma = 1.745$) and (*d*) $Wo = 2.15$ ($\gamma = 14.6$).

The results in figure 6 show a good agreement between the theory of the primary pressure oscillations $P_0(Z, T)$ and the experimental measurements over a wide range of Wo and γ. We observe that the agreement between theory and experiment is better for $0.1 < \gamma < 1$ than for $\gamma > 1$. This deviation can be attributed to the fact that for larger values of $\gamma > 1$, the combined effect of compliance and oscillations is strong, and the time it takes the top wall to adjust to the flow oscillations becomes much longer than the oscillation time scale, localising the majority of the pressure variation near the channel's inlet. This rapid, localised variation is more challenging to capture using equally spaced pressure ports in the experiments. Nevertheless, the overall agreement between theory and experiment on the trend of $P_0(Z, T)$ and how it changes with Wo and γ is good, thus not only validating the predicted nonlinear pressure distribution (4.8) but also providing the first experimental demonstration of the strong coupling between flow oscillations and wall deformations, even in weakly compliant channels ($\beta \ll 1$).

5.3. *Comparison of streaming pressure profiles in deformable channels*

Next, we turn to the elastoinertial rectification phenomenon, namely the theoretical prediction that $\langle P \rangle / \beta \equiv \langle P_1 \rangle \neq 0$ due to the nonlinear coupling of the flow's inertia with

https://doi.org/10.1017/jfm.2025.10771 Published online by Cambridge University Press

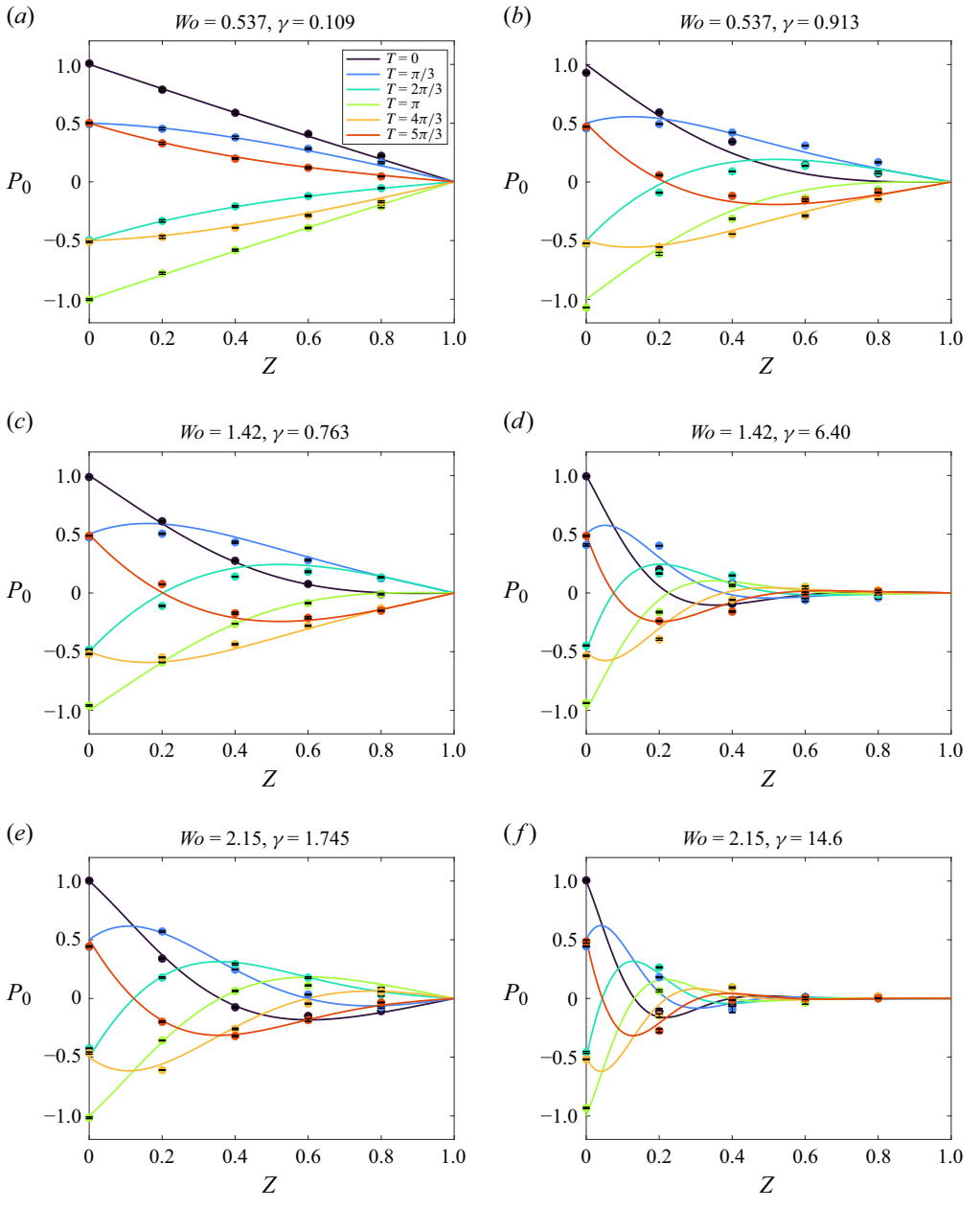


Figure 6. Comparison of the dimensionless axial pressure distribution in a deformable channel between experiment (symbols) and theory (solid curves), i.e. $P_0(Z,T) = \mathrm{Re}[P_{0,a}(Z)\mathrm{e}^{\mathrm{i}T}]$ based on (4.8), with (*a*) $Wo = 0.537$ ($\beta = 0.0208$), (*b*) $Wo = 0.537$ ($\beta = 0.164$), (*c*) $Wo = 1.42$ ($\beta = 0.02$), (*d*) $Wo = 1.42$ ($\beta = 0.125$), (*e*) $Wo = 2.15$ ($\beta = 0.0167$) and (*f*) $Wo = 2.15$ ($\beta = 0.104$). The evolution of the pressure distribution is shown over a full cycle (thus $T = 2\pi$ overlaps $T = 0$).

the wall deformation (§ 4.2). All data shown in this section are based on deionised water as the working fluid. To this end, in figure 7, we compare the streaming pressure $\langle P_1 \rangle(Z)$ calculated numerically from (4.20) (as described above) with the corresponding quantity extracted from the experiments.

https://doi.org/10.1017/jfm.2025.10771 Published online by Cambridge University Press

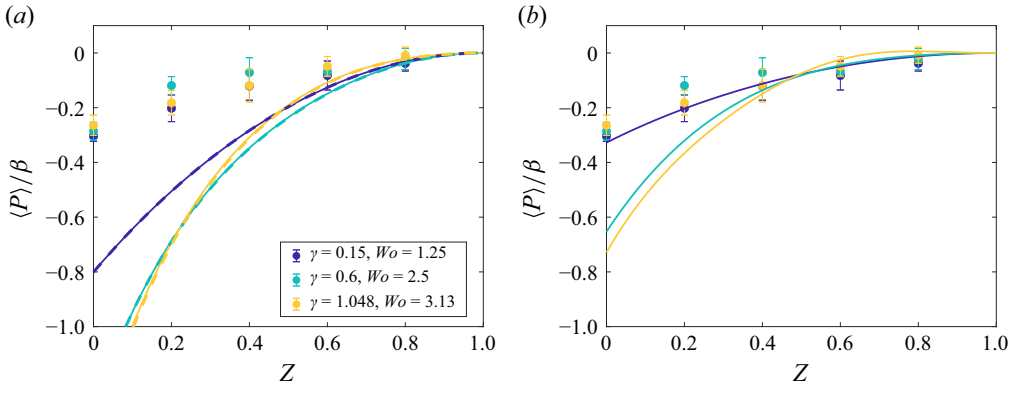


Figure 7. (*a*) Comparison of streaming pressure (cycle-averaged pressure) distribution, $\langle P\rangle/\beta = \langle P_1\rangle$, between the experimental data (symbols), the theoretical prediction based on numerically evaluating (4.20) (solid curves) and the closed-form approximation (A7) (dashed curves, overlapping the solid curves) in a deformable channel with $\beta \approx 0.17$ and $\gamma = 0.15$ ($Wo = 1.25$), $\gamma = 0.6$ ($Wo = 2.5$) and $\gamma = 1.048$ ($Wo = 3.13$) achieved by changing the input frequency in the same channel. (*b*) *Ad hoc* modification of the theory by multiplying the effective slip term in (4.19) by 0.4 to demonstrate the sensitivity of the streaming pressure to the effective slip contribution.

This comparison is more challenging than the previous one in § 5.2 because we are now dealing with small quantities that are $O(\beta)$. Consequently, the error bars on the experimental data in figure 7 are much larger as the pressure values being measured push the experimental system to its sensitivity limit. Nevertheless, in figure 7(*a*), we see a reasonable agreement between experiment and theory regarding the trend of the streaming pressure distribution along the channel. Interestingly, $\langle P_1\rangle$ is less sensitive to γ under the present flow conditions, and both the theory curves and experimental data cluster together.

The largest disagreement is at $Z = 0$, at the first pressure port, which may be expected as this is the location in the experimental system that is least likely to satisfy all the assumptions of the theory. Specifically, as shown in figure 2, there is a rigid section attached to the inlet of the deformable channel in the experiments, which constrains the displacement along the inlet plane. However, this possibility is not accounted for in the theory – the leading-order equation (2.8) for the displacement does not allow for BCs to be imposed in Z and thus cannot capture this localised clamping at the inlet, which previous work showed is confined to a 'boundary layer' of thickness $O(\sqrt{w/\ell})$ (Wang & Christov 2021). While the inlet conditions on the displacement have no discernible effect on $P_0(Z)$, as demonstrated in § 5.2 by the excellent agreement between theory and experiments at $Z = 0$, these conditions may affect the weaker effects being investigated at $O(\beta)$.

To test the hypothesis that the inlet conditions may affect the agreement there, we turn to (4.19) and (4.20), from which we observe that the streaming pressure is generated by a competition between effective wall slip (at the location of the undeformed wall) and advective inertia. Specifically, the effective slip is a direct function of the displacement, per (4.15). Therefore, we expect this $O(\beta)$ quantity to be possibly strongly affected by the inlet restrictions in the experiments. Specifically, if the displacement in the experiments near the inlet is constrained, or otherwise reduced, then this term might be overestimated by the theory. To test this hypothesis, we check the sensitivity of the $\langle P_1\rangle(Z)$ profile to the magnitude of the effective slip term. We find that even approximately halving this term

https://doi.org/10.1017/jfm.2025.10771 Published online by Cambridge University Press

can account for much of the disagreement between theory and experiment, especially as $Z \to 0$, as shown by the *ad hoc* modification in figure 7(*b*).

Though the *ad hoc* modification improves the agreement to quite an extent for the lowest frequency (lowest *Wo* and γ values), it still exhibits disagreement for the larger frequencies (larger *Wo* and γ values). In fact, fully suppressing the effective slip term brings the streaming pressures at the higher frequency even closer to the experimental data points. To further investigate the frequency-dependent nature of this agreement/disagreement, we would need to better assess how well our theory models the effective slip term in (4.19). The present theory evaluates this term using the result that $U_{Y,0} \propto P_0$, per (4.15), and the shear $\partial V_{Z,0}/\partial Y$ based on (4.3). We would need a more advanced experimental set-up, which measures the velocity field and the deformation independently, to evaluate the accuracy of each of these results. Alternatively, measuring just the slip velocity at $Y = 1$ experimentally, say using particle image velocimetry, and comparing it with (4.10*b*) could be another independent check. These directions will be pursued in forthcoming investigations.

Despite the limitations and challenges of these measurements, the experimental data appear to capture the key effects of *Wo* and γ on the streaming pressure profile, including the non-monotonic behaviour with respect to γ (in particular for $Z > 0.5$), though admittedly, the error bars on the experimental measurements for different γ overlap.

6. Conclusion

We presented a systematic, combined theoretical and experimental investigation of two-way coupling between oscillatory internal viscous flows and deformable confining boundaries. Specifically, we provided a theory (and solutions) for the pressure distribution due to oscillatory flow in a 3-D channel with a deformable top wall, its relation to the flow rate in terms of complex-valued functions, as well as the shape of the deformation of the compliant wall, taking into account its thickness. Consistent with microfluidics-oriented applications, we assumed the channels were shallow and slender, which allowed the use of the lubrication approximation. However, as convective inertia cannot be eliminated from the axial momentum equation, we also assumed a small compliance number to make progress on the nonlinearly coupled problem, unlike steady (Christov *et al.* 2018) and startup (Martínez-Calvo *et al.* 2020) flow-induced deformation problems previously analysed. However, we did not make assumptions on the two key dimensionless groups involving the oscillation frequency, the Womersley number and the elastoviscous number, the latter being the key controlling parameter of this type of 'viscous–elastic' structure interaction problem (Elbaz & Gat 2014). To validate the theory, we designed a PDMS-based microfluidic experimental platform capable of measuring the pressure distribution in these flows.

Our key findings are that the primary (periodic) pressure distribution from the theory shows strong agreement with the experimental measurements. Furthermore, we were able to measure (albeit with higher uncertainty) the weak, secondary (cycle-averaged, streaming) pressure distribution predicted by the theory. The resulting comparison shows agreement in the trends and thus provides the first experimental demonstration of elastoinertial rectification due to oscillatory flow in 3-D deformable channels, which is a subtle effect not previously measured in experiments. Our theoretical–experimental results demonstrate that, as Zhang & Rallabandi (2024) recently clarified, geometric nonlinearity due to the deformation of the channel and inertial nonlinearity due to the advective inertia of the fluid, are inextricably coupled in determining the pressure characteristics of these

https://doi.org/10.1017/jfm.2025.10771 Published online by Cambridge University Press

flows. Our work thus advances the fundamental understanding of soft hydraulics involving oscillatory flows. Notably, there are no fitting parameters in the theory; each property of the fluid, the deformable wall and the geometry was experimentally characterised. Consequently, the theory of elastoinertial rectification in 3-D deformable channels is ready for use in applications.

In the future, it would be worth pursuing the experimental measurement of the phasing between the flow rate and the primary pressure (gradient), recently explored in tubes through simulations by Krul & Bagchi (2025), as well as the direct measurement of the elastic wall's deformation profile. Although our experiments showed negligible effect of the deformable wall's inertia, solving for the displacement profile for finite St_s in (2.8) would be relevant for applications to soft robotics (Gamus *et al.* 2018). In addition, many relevant working fluids for applications, such as polymer solutions, colloidal suspensions and biological fluids, show non-Newtonian rheology (Chhabra & Richardson 2008; Roselli & Diller 2011), which will introduce another set of nonlinear couplings beyond those already understood in steady flow (Christov 2022; Boyko & Christov 2023; Chun *et al.* 2024), between the fluid rheology (e.g. viscoelastic stresses or changes of the apparent viscosity due to shear-thinning), flow oscillations and wall deformation. Further investigation of oscillatory flows of complex fluid in deformable channels, especially viscoelastic ones (Asghari *et al.* 2020), will be relevant to microfluidic-oriented applications (Dincau *et al.* 2020; Mudugamuwa *et al.* 2024). Another avenue of future work could be to revisit the possibility of flow rectification due to oscillatory flow in deformable poroelastic media (Fiori, Pramanik & MacMinn 2023).

Acknowledgements. We thank B. Rallabandi for many insightful discussions on elastoinertial rectification and J. Coonley for experimental assistance.

Funding. J.F. acknowledges partial support by the US National Science Foundation under grant no. CBET-2323045. I.C.C. acknowledges partial support by the US National Science Foundation under grant no. CMMI-2245343.

Declaration of interests. The authors report no conflict of interest.

Appendix A. Closed-form approximations for the streaming quantities, and limits

In § 4, we solved the linear BVP (4.17) numerically since the left-hand side of the ordinary differential equation is an unwieldy expression involving complex-valued quantities. Zhang & Rallabandi (2024) used an approximation procedure, similar to the one used to derive reduced models of cardiovascular flows (see e.g. van de Vosse & Stergiopulos 2011), that leads to closed-form, albeit *ad hoc* (unless $Wo \ll 1$), expressions. The procedure consists of replacing the Womersley profile (4.3) with a Poiseuille profile with the same centreline velocity. In the present context, the approximation takes the form

$$\left.\begin{aligned} V_{Z,0,a}(Y,\,Z) &\approx 4\mathfrak{v}(Wo)Y(1-Y)\left(-\frac{\mathrm{d}P_{0,a}}{\mathrm{d}Z}\right), \\ \mathfrak{v}(Wo) &\overset{\text{def}}{=} \frac{1}{\mathrm{i}Wo^2}\left[1-\frac{1}{\cos\left(\mathrm{i}^{3/2}Wo/2\right)}\right]. \end{aligned}\right\} \tag{A1}$$

Substituting (A1) into (2.4*a*), we find the approximate vertical velocity component:

$$V_{Y,0,a}(Y,\,Z) \approx \mathfrak{v}(Wo)\left(2Y^2-\frac{4Y^3}{3}\right)\kappa(Wo,\,\gamma,\,\mathscr{T})^2 P_{0,a}(Z), \tag{A2}$$

https://doi.org/10.1017/jfm.2025.10771 Published online by Cambridge University Press

having used (4.7) to replace $\mathrm{d}^2 P_{0,a}/\mathrm{d}Z^2$ by $\kappa^2 P_{0,a}$. Using (A1) and (A2), and carefully tracking the conjugation in evaluating the time averages of phasors, we find an approximate solution of the BVP (4.17):

$$\widetilde{\langle\!\langle V_{Z,1}\rangle\!\rangle}(Y,\,Z) \approx \frac{Wo^2}{\gamma}\frac{1}{2}\mathrm{Re}\left[|\mathfrak{v}|^2\frac{\mathrm{d}P_{0,a}}{\mathrm{d}Z}(\kappa^2)^* P_{0,a}^*\right]\frac{2}{45}(4Y^6 - 12Y^5 + 15Y^4 - 7Y). \quad \text{(A3)}$$

Note that the approximate velocity profile (A1)–(A2) is used only for evaluating the advective terms to obtain the closed-form solution (A3). The slip velocity (4.15) can be calculated without approximation by using (4.3) in (4.15), to find

$$\left\langle P_0\frac{\partial V_{Z,0}}{\partial Y}\bigg|_{Y=1}\right\rangle = \frac{1}{2}\mathrm{Re}\left[P_{0,a}^*\frac{\mathrm{i}^{1/2}}{Wo}\tan\left(\mathrm{i}^{3/2}Wo/2\right)\left(-\frac{\mathrm{d}P_{0,a}}{\mathrm{d}Z}\right)\right]. \quad \text{(A4)}$$

Now, substituting (A3) and (A4) into (4.19), we obtain

$$\mathfrak{Q}(Z) \approx -(1+\mathscr{T})\mathrm{Re}\left[\mathfrak{q}(Wo)\frac{\mathrm{d}P_{0,a}}{\mathrm{d}Z}P_{0,a}^*\right], \quad \text{(A5)}$$

where

$$\begin{aligned}\mathfrak{q}(Wo) &\overset{\text{def}}{=} -\left[\frac{\mathrm{i}^{1/2}}{4Wo}\tan\left(\mathrm{i}^{3/2}Wo/2\right) + \frac{3Wo^2}{70}\mathrm{i}\frac{|\mathfrak{v}(Wo)|^2}{\mathfrak{f}(Wo)^*}\right] \\ &= \begin{cases}\dfrac{1}{8} - \mathrm{i}\dfrac{31}{1680}Wo^2 - \dfrac{31}{16\,800}Wo^4 + O(Wo^6), & Wo \to 0,\\ \dfrac{3}{70} + \dfrac{(35\mathrm{i}+12)\mathrm{i}^{1/2}}{140}Wo^{-1} + O(Wo^{-2}), & Wo \to \infty.\end{cases}\end{aligned} \quad \text{(A6)}$$

Recall that $\mathfrak{v}(Wo)$ is defined in (A1) and $\mathfrak{f}(Wo)$ is defined (4.4). Notice that $\mathfrak{Q}$ depends on γ only through $P_{0,a}$. Within $\mathfrak{q}$, the first term in the parentheses arises from effective slip at the original location of the deformable wall (no approximation), while the second term is the contribution of advective inertia (approximated based on (A1)–(A2)).

Based on (A5), we compute $\int_Z^1 \mathfrak{Q}(\tilde{Z})\,\mathrm{d}\tilde{Z}$ and (4.20) becomes

$$\begin{aligned}\langle P_1\rangle(Z) \approx{}& -12(1+\mathscr{T}) \\ &\times \mathrm{Re}\left\{\mathfrak{q}(Wo)\frac{\kappa}{2|\sinh\kappa|^2}\left[\frac{\sinh^2\left((1-Z)\mathrm{Re}[\kappa]\right)}{\mathrm{Re}[\kappa]} - \mathrm{i}\frac{\sin^2\left((1-Z)\mathrm{Im}[\kappa]\right)}{\mathrm{Im}[\kappa]}\right]\right\}.\end{aligned} \quad \text{(A7)}$$

The comparisons in figure 7(*a*) show that this *ad hoc* approximation is actually extremely accurate across a range of γ and Wo values.

In the 'quasi-rigid limit' (Zhang & Rallabandi 2024), $\gamma \to 0$, a simpler expression can be obtained since κ, $\mathrm{Re}[\kappa]$, $\mathrm{Im}[\kappa] \sim \sqrt{\gamma} \to 0$, namely

$$\langle P_1\rangle(Z) \approx -6\,(1+\mathscr{T})\,\mathrm{Re}[\mathfrak{q}(Wo)](1-Z)^2, \qquad \gamma \to 0. \quad \text{(A8)}$$

References

Amselem, G., Clanet, C. & Benzaquen, M. 2023 Valveless pumping at low Reynolds numbers. *Phys. Rev. Appl.* **19**, 024017.

Anand, V. & Christov, I.C. 2020 Transient compressible flow in a compliant viscoelastic tube. *Phys. Fluids* **32**, 112014.

https://doi.org/10.1017/jfm.2025.10771 Published online by Cambridge University Press

ANAND, V., MUCHANDIMATH, S.C. & CHRISTOV, I.C. 2020 Hydrodynamic bulge testing: materials characterization without measuring deformation. *ASME J. Appl. Mech.* **87**, 051012.

ASGHARI, M., CAO, X., MATEESCU, B., VAN LEEUWEN, D., ASLAN, M.K., STAVRAKIS, S. & DEMELLO, A.J. 2020 Oscillatory viscoelastic microfluidics for efficient focusing and separation of nanoscale species. *ACS Nano* **14**, 422–433.

BATTAT, S., WEITZ, D.A. & WHITESIDES, G.M. 2022 Nonlinear phenomena in microfluidics. *Chem. Rev.* **122**, 6921–6937.

BHATIA, S.N. & INGBER, D.E. 2014 Microfluidic organs-on-chips. *Nat. Biotechnol.* **32**, 760–772.

BHOSALE, Y., PARTHASARATHY, T. & GAZZOLA, M. 2022 Soft streaming – flow rectification via elastic boundaries. *J. Fluid Mech.* **945**, R1.

BIVIANO, M.D., PALUDAN, M.V., CHRISTENSEN, A.H., ØSTERGAARD, E.V. & JENSEN, K.H. 2022 Smoothing oscillatory peristaltic pump flow with bioinspired passive components. *Phys. Rev. Appl.* **18**, 064013.

BORK, P.A.R., LADRÓN-DE GUEVARA, A., CHRISTENSEN, A.H., JENSEN, K.H., NEDERGAARD, M. & BOHR, T. 2023 Astrocyte endfeet may theoretically act as valves to convert pressure oscillations to glymphatic flow. *J. R. Soc. Interface* **20**, 20230050.

BOYKO, E. & CHRISTOV, I.C. 2023 Non-Newtonian fluid–structure interaction: flow of a viscoelastic Oldroyd-B fluid in a deformable channel. *J. Non-Newtonian Fluid Mech.* **313**, 104990.

BOYKO, E., STONE, H.A. & CHRISTOV, I.C. 2022 Flow rate-pressure drop relation for deformable channels via fluidic and elastic reciprocal theorems. *Phys. Rev. Fluids* **7**, L092201.

BRUUS, H. 2008 *Theoretical Microfluidics*. Oxford University Press.

BURTON, A.C. 1952 Laws of physics and flow in blood vessels. In *Ciba Foundation Symposium–Visceral Circulation*, (ed. G.E.W. Wolstenholme), pp. 70–86.

ČANIĆ, S., LAMPONI, D., MIKELIĆ, A. & TAMBAČA, J. 2005 Self-consistent effective equations modeling blood flow in medium-to-large compliant arteries. *Multiscale Model. Simul.* **3**, 559–596.

RODRÍGUEZ DE CASTRO, A., CHABANON, M. & GOYEAU, B. 2023 Numerical analysis of the fluid-solid interactions during steady and oscillatory flows of non-Newtonian fluids through deformable porous media. *Chem. Eng. Res. Des.* **193**, 38–53.

CHALLAMEL, N. & ELISHAKOFF, I. 2019 A brief history of first-order shear-deformable beam and plate models. *Mech. Res. Commun.* **102**, 103389.

CHEUNG, P., TODA-PETERS, K. & SHEN, A.Q. 2012 In situ pressure measurement within deformable rectangular polydimethylsiloxane microfluidic devices. *Biomicrofluidics* **6**, 026501.

CHHABRA, R.P. & RICHARDSON, J.F. 2008 *Non-Newtonian Flow and Applied Rheology*. 2nd edn. Butterworth-Heinemann.

CHRISTOV, I.C. 2022 Soft hydraulics: from Newtonian to complex fluid flows through compliant conduits. *J. Phys.: Condens. Matter* **34**, 063001.

CHRISTOV, I.C., COGNET, V., SHIDHORE, T.C. & STONE, H.A. 2018 Flow rate–pressure drop relation for deformable shallow microfluidic channels. *J. Fluid Mech.* **814**, 267–286.

CHUN, S., BOYKO, E., CHRISTOV, I.C. & FENG, J. 2024 Flow rate–pressure drop relations for shear-thinning fluids in deformable configurations: theory and experiments. *Phys. Rev. Fluids* **9**, 043302.

CUI, S., BHOSALE, Y. & GAZZOLA, M. 2024 Three-dimensional soft streaming. *J. Fluid Mech.* **979**, A7.

DALSBECKER, P., BECK ADIELS, C. & GOKSÖR, M. 2022 Liver-on-a-chip devices: the pros and cons of complexity. *Am. J. Physiol. Gastrointest.* **323**, G188–G204.

DINCAU, B., DRESSAIRE, E. & SAURET, A. 2020 Pulsatile flow in microfluidic systems. *Small* **16**, 1904032.

DÖRNER, P., SCHRÖDER, W. & KLAAS, M. 2021 Experimental quantification of oscillating flow in finite-length straight elastic vessels for Newtonian and non-Newtonian fluids. *Eur. J. Mech. B Fluids* **87**, 180–195.

DOWSON, D. & JIN, Z.-M. 1986 Micro-elastohydrodynamic lubrication of synovial joints. *Eng. Med.* **15**, 63–65.

DRAGON, C.A. & GROTBERG, J.B. 1991 Oscillatory flow and mass transport in a flexible tube. *J. Fluid Mech.* **231**, 135–155.

ELBAZ, S.B. & GAT, A.D. 2014 Dynamics of viscous liquid within a closed elastic cylinder subject to external forces with application to soft robotics. *J. Fluid Mech.* **758**, 221–237.

FIORI, M., PRAMANIK, S. & MACMINN, C.W. 2023 Flow and deformation due to periodic loading in a soft porous material. *J. Fluid Mech.* **974**, A2.

FUNG, Y.C. 1997 *Biomechanics: Circulation*. 2nd edn. Springer-Verlag.

GAMUS, B., SALEM, L., BEN-HAIM, E., GAT, A.D. & OR, Y. 2018 Interaction between inertia, viscosity, and elasticity in soft robotic actuator with fluidic network. *IEEE Trans. Robotics* **34**, 81–90.

https://doi.org/10.1017/jfm.2025.10771 Published online by Cambridge University Press

GAN, Y., HOLSTEIN-RØNSBO, S., NEDERGAARD, M., BOSTER, K.A.S., THOMAS, J.H. & KELLEY, D.H. 2023 Perivascular pumping of cerebrospinal fluid in the brain with a valve mechanism. *J. R. Soc. Interface* **20**, 20230288.

GERVAIS, T., EL-ALI, J., GÜNTHER, A. & JENSEN, K.F. 2006 Flow-induced deformation of shallow microfluidic channels. *Lab Chip* **6**, 500–507.

GROTBERG, J.B. 1994 Pulmonary flow and transport phenomena. *Annu. Rev. Fluid Mech.* **26**, 529–571.

GROTBERG, J.B. & JENSEN, O.E. 2004 Biofluid mechanics in flexible tubes. *Annu. Rev. Fluid Mech.* **36**, 121–147.

HEIL, M. & HAZEL, A.L. 2011 Fluid-structure interaction in internal physiological flows. *Annu. Rev. Fluid Mech.* **43**, 141–162.

HOWELL, P., KOZYREFF, G. & OCKENDON, J. 2009 *Applied Solid Mechanics*. Cambridge University Press.

INAMDAR, T.C., WANG, X. & CHRISTOV, I.C. 2020 Unsteady fluid-structure interactions in a soft-walled microchannel: a one-dimensional lubrication model for finite Reynolds number. *Phys. Rev. Fluids* **5**, 064101.

JEONG, I.C., BYCHKOV, D. & SEARSON, P.C. 2018 Wearable devices for precision medicine and health state monitoring. *IEEE Trans. Biomed. Eng.* **66**, 1242–1258.

KARAN, P., CHAKRABORTY, J. & CHAKRABORTY, S. 2021 Generalization of elastohydrodynamic interactions between a rigid sphere and a nearby soft wall. *J. Fluid Mech.* **923**, A32.

KIERZENKA, J. & SHAMPINE, L.F. 2001 A BVP solver based on residual control and the Maltab PSE. *ACM Trans. Math. Softw.* **27**, 299–316.

KRUL, O. & BAGCHI, P. 2025 Pulsatile flow in a thin-walled viscoelastic tube. *J. Fluid Mech.* **1007**, A82.

KU, D.N. 1997 Blood flow in arteries. *Annu. Rev. Fluid Mech.* **29**, 399–434.

KURZEJA, P., STEEB, H., STRUTZ, M.A. & RENNER, J. 2016 Oscillatory fluid flow in deformable tubes: implications for pore-scale hydromechanics from comparing experimental observations with theoretical predictions. *J. Acoust. Soc. Am.* **140**, 4378–4395.

KWON, K. *et al.* 2023 A battery-less wireless implant for the continuous monitoring of vascular pressure, flow rate and temperature. *Nat. Biomed. Eng.* **7**, 1215–1228.

LAMBERT, J.W. 1958 On the nonlinearities of fluid flow in nonrigid tubes. *J. Frankl. Inst.* **266**, 83–102.

LEAL, L.G. 2007 *Advanced Transport Phenomena: Fluid Mechanics and Convective Transport Processes*, Cambridge Series in Chemical Engineering, vol. 7. Cambridge University Press.

LEBOVITZ, N.R. 1982 Perturbation expansions on perturbed domains. *SIAM Rev.* **24**, 381–400.

LESLIE, D.C., EASLEY, C.J., SEKER, E., KARLINSEY, J.M., UTZ, M., BEGLEY, M.R. & LANDERS, J.P. 2009 Frequency-specific flow control in microfluidic circuits with passive elastomeric features. *Nat. Phys.* **5**, 231–235.

LEUNG, C.M. *et al.* 2022 A guide to the organ-on-a-chip. *Nat. Rev. Methods Primers* **2**, 33.

LEVENSTEIN, M.A. *et al.* 2022 Millimeter-scale topography facilitates coral larval settlement in wave-driven oscillatory flow. *PLoS One* **17**, e0274088.

LIND, J.U. *et al.* 2017 Instrumented cardiac microphysiological devices via multimaterial three-dimensional printing. *Nat. Mat.* **16**, 303–308.

LING, S.C. & ATABEK, H.B. 1972 A nonlinear analysis of pulsatile flow in arteries. *J. Fluid Mech.* **55**, 493.

MARTÍNEZ-CALVO, A., SEVILLA, A., PENG, G.G. & STONE, H.A. 2020 Start-up flow in shallow deformable microchannels. *J. Fluid Mech.* **885**, A25.

MATIA, Y., ELIMELECH, T. & GAT, A.D. 2017 Leveraging internal viscous flow to extend the capabilities of beam-shaped soft robotic actuators. *Soft Robot.* **4**, 126–134.

MATIA, Y., KAISER, G.H., SHEPHERD, R.F., GAT, A.D., LAZARUS, N. & PETERSEN, K.H. 2023 Harnessing nonuniform pressure distributions in soft robotic actuators. *Adv. Intell. Syst.* **5**, 2200330.

MCDONALD, D.A. 1955 The relation of pulsatile pressure to flow in arteries. *J. Physiol.* **127**, 533–552.

MEHBOUDI, A. & YEOM, J. 2019 Experimental and theoretical investigation of a low-Reynolds-number flow through deformable shallow microchannels with ultra-low height-to-width aspect ratios. *Microfluid. Nanofluid.* **23**, 66.

MENON, K., HU, Z. & MARSDEN, A.L. 2024 Cardiovascular fluid dynamics: a journey through our circulation. *Flow* **4**, E7.

MINDLIN, R.D. 1951 Influence of rotatory inertia and shear on flexural motions of isotropic, elastic plates. *ASME J. Appl. Mech.* **18**, 31–38.

MOSADEGH, B., KUO, C.-H., TUNG, Y.-C., TORISAWA, Y.-S., BERSANO-BEGEY, T., TAVANA, H. & TAKAYAMA, S. 2010 Integrated elastomeric components for autonomous regulation of sequential and oscillatory flow switching in microfluidic devices. *Nat. Phys.* **6**, 433–437.

https://doi.org/10.1017/jfm.2025.10771 Published online by Cambridge University Press

MUDUGAMUWA, A., ROSHAN, U., HETTIARACHCHI, S., CHA, H., MUSHARAF, H., KANG, X., TRINH, Q.T., XIA, H.M., NGUYEN, N.-T. & ZHANG, J. 2024 Periodic flows in microfluidics*Small* **20**, 2404685.
OZSUN, O., YAKHOT, V. & EKINCI, K.L. 2013 Non-invasive measurement of the pressure distribution in a deformable micro-channel. *J. Fluid Mech.* **734**, R1.
PALUDAN, M.V., DOLLET, B., MARMOTTANT, P. & JENSEN, K.H. 2024 Elastohydrodynamic interactions in soft hydraulic knots. *J. Fluid Mech.* **984**, A55.
PANDE, S.D., WANG, X. & CHRISTOV, I.C. 2023 Oscillatory flows in compliant conduits at arbitrary Womersley number. *Phys. Rev. Fluids* **8**, 124102.
PARTHASARATHY, T., BHOSALE, Y. & GAZZOLA, M. 2022 Elastic solid dynamics in a coupled oscillatory Couette flow system. *J. Fluid Mech.* **946**, A15.
PEDLEY, T.J. 1980 *The Fluid Mechanics of Large Blood Vessels*. Cambridge University Press.
PIELHOP, K., KLAAS, M. & SCHRÖDER, W. 2012 Analysis of the unsteady flow in an elastic stenotic vessel. *Eur. J. Mech. B Fluids* **35**, 102–110.
PIELHOP, K., KLAAS, M. & SCHRÖDER, W. 2015 Experimental analysis of the fluid–structure interaction in finite-length straight elastic vessels. *Eur. J. Mech. B Fluids* **50**, 71–88.
RAJ, M., DASGUPTA, K.S. & CHAKRABORTY, S. 2019 Biomimetic pulsatile flows through flexible microfluidic conduits. *Biomicrofluidics* **13**, 014103.
RALLABANDI, B. 2024 Fluid-elastic interactions near contact at low Reynolds number. *Annu. Rev. Fluid Mech.* **56**, 491–519.
RAMACHANDRA RAO, A. 1983 Oscillatory flow in an elastic tube of variable cross-section. *Acta Mech.* **46**, 155–165.
RAMOS-ARZOLA, L. & BAUTISTA, O. 2021 Fluid structure-interaction in a deformable microchannel conveying a viscoelastic fluid. *J. Non-Newtonian Fluid Mech.* **296**, 104634.
REDDY, J.N. 2007 *Theory and Analysis of Elastic Plates and Shells*. 2nd edn. CRC Press.
REISSNER, E. 1945 The effect of transverse shear deformation on the bending of elastic plates. *ASME J. Appl. Mech.* **12**, A68–A77.
RILEY, N. 1998 Acoustic streaming. *Theor. Comp. Fluid Dyn.* **10**, 349–356.
RILEY, N. 2001 Steady treaming. *Annu. Rev. Fluid Mech.* **33**, 43–65.
ROMANÒ, F., SURESH, V., GALIE, P.A. & GROTBERG, J.B. 2020 Peristaltic flow in the glymphatic system. *Sci. Rep.* **10**, 21065.
ROSELLI, R.J. & DILLER, K.R. 2011 *Biotransport: Principles and Applications*. Springer.
SADHAL, S.S. 2012 Acoustofluidics 13: analysis of acoustic streaming by perturbation methods. *Lab Chip* **12**, 2292–2300.
SELVEROV, K.P. & STONE, H.A. 2001 Peristaltically driven channel flows with applications toward micromixing. *Phys. Fluids* **13**, 1837–1859.
SHIDHORE, T.C. & CHRISTOV, I.C. 2018 Static response of deformable microchannels: a comparative modelling study. *J. Phys.: Condens. Matter* **30**, 054002.
STEWART, P.S. & FOSS, A.J.E. 2019 Self-excited oscillations in a collapsible channel with applications to retinal venous pulsation. *ANZIAM J.* **61**, 320–348.
TAKAGI, D. & BALMFORTH, N.J. 2011 Peristaltic pumping of viscous fluid in an elastic tube. *J. Fluid Mech.* **672**, 196–218.
TREVINO, A., POWERS, T.R., ZENIT, R. & RODRIGUEZ, M. 2025 Low Reynolds number pumping near an elastic half space. *Phys. Rev. Fluids* **10**, 054003.
VISHWANATHAN, G. & JUAREZ, G. 2020 Generation and application of sub-kilohertz oscillatory flows in microchannels. *Microfluid. Nanofluidics* **24**, 69.
VISHWANATHAN, G. & JUAREZ, G. 2022 Assembly and characterization of an external driver for the generation of sub-kilohertz oscillatory flow in microchannels. *J. Vis. Exp.* **179**, e63294.
VISHWANATHAN, G. & JUAREZ, G. 2023 Synchronous oscillatory electro-inertial focusing of microparticles. *Biomicrofluidics* **17**, 064105.
VAN DE VOSSE, F.N. & STERGIOPULOS, N. 2011 Pulse wave propagation in the arterial tree. *Annu. Rev. Fluid Mech.* **43**, 467–499.
WANG, X. & CHRISTOV, I.C. 2021 Reduced models of unidirectional flows in compliant rectangular ducts at finite Reynolds number. *Phys. Fluids* **33**, 102004.
WARD, T.J. & WHITTAKER, R.J. 2019 Effect of base-state curvature on self-excited high-frequency oscillations in flow through an elastic-walled channel. *Phys. Rev. Fluids* **4**, 113901.
WOMERSLEY, J.R. 1955*a* Method for the calculation of velocity, rate of flow and viscous drag in arteries when the pressure gradient is known. *J. Physiol.* **127**, 553–563.
WOMERSLEY, J.R. 1955*b* XXIV. Oscillatory motion of a viscous liquid in a thin-walled elastic tube—I: the linear approximation for long waves. *Phil. Mag Ser.* **7 46**, 199–221.

https://doi.org/10.1017/jfm.2025.10771 Published online by Cambridge University Press

WOMERSLEY, J.R. 1957 Oscillatory flow in arteries: the constrained elastic tube as a model of arterial flow and pulse transmission. *Phys. Med. Biol.* **2**, 178–187.

XIA, H.M., WU, J.W., ZHENG, J.J., ZHANG, J. & WANG, Z.P. 2021 Nonlinear microfluidics: device physics, functions, and applications. *Lab Chip* **21**, 1241–1268.

XU, S., NUNEZ, C.M., SOURI, M. & WOOD, R.J. 2023 A compact DEA-based soft peristaltic pump for power and control of fluidic robots. *Sci. Robot.* **8**, eadd4649.

ZAMIR, M. 2000 *The Physics of Pulsatile Flow*. Springer.

ZHANG, X. & RALLABANDI, B. 2024 Elasto-inertial rectification of oscillatory flow in an elastic tube. *J. Fluid Mech.* **996**, A16.

ZIENKIEWICZ, O.C., TAYLOR, R.L. & ZHU, J.Z. 2013 *The Finite Element Method: Its Basis and Fundamentals*. 7th edn. Butterworth-Heinemann.

https://doi.org/10.1017/jfm.2025.10771 Published online by Cambridge University Press